

UC Berkeley

UC Berkeley Electronic Theses and Dissertations

Title

Advances in 3ω Measurements to Spatially Track a Moving Interface

Permalink

<https://escholarship.org/uc/item/07q0t871>

Author

Hodges, Wyatt

Publication Date

2019

Peer reviewed|Thesis/dissertation

Advances in 3ω Measurements to Spatially Track a Moving Interface

By Wyatt Hodges

A dissertation submitted in partial satisfaction of the

requirements for the degree

of

Doctor of Philosophy

Mechanical Engineering

and the Designated Emphasis

in

Energy Science and Technology – Heat Transfer

in the

Graduate Division

of the

University of California, Berkeley

Committee in charge:

Professor Chris Dames, Chair

Professor Costas Grigoropoulos

Professor James Analytis

Spring 2019

Advances in 3 ω Measurements to Spatially Track a Moving Interface

© 2019

By Wyatt Hodges

Abstract

Advances in 3ω Measurements to Spatially Track a Moving Interface

By Wyatt Hodges

Doctor of Philosophy in Engineering – Mechanical Engineering

University of California, Berkeley

Professor Christopher Dames, Chair

Detecting depth varying thermal properties is desirable for applications such as cryosurgery, landmine detection and non-destructive testing. This can be accomplished by periodic heating, exploiting the resulting frequency dependent penetration depth. Using this, objects with thermal conductivity distinct from their surroundings (such as material flaws or landmines) can be detected. In cryosurgery, for treatment of atrial fibrillation, it is desirable to track the location of moving boundaries between two phases (i.e. frozen and thawed tissue) with sub-millimeter precision. This spatial resolution is not attainable with conventional imaging.

In this dissertation, the 3ω thermal property measurement technique is used to make new types of measurements on systems changing in real time. Analytical understanding of measurements with multiple frequency excitations is first developed, and verified with experiments. Next, the 3ω technique is used to sense thickness of samples (200 μm and 500 μm ice). The same sensors are used to detect step changes in thermal properties, including phase change, of water and mouse liver samples in real time. Finally an experimental setup is constructed to track an oil-air interface as it moves. Numerical modeling is used to convert measured 3ω voltages into spatial dimensions. For slow front velocities, the location of the oil-air front determined from the 3ω approach is found to be accurate to within an average error of under 18 μm (RMS) for front distances between 12 and 360 μm .

Table of Contents

Table of Contents	i
List of Figures	ii
List of Tables	v
Acknowledgements.....	vi
I. Introduction	1
a. Resistance thermometry.....	2
b. 3ω measurements.....	3
c. Lock-in amplifier.....	5
d. Experimental setup	6
e. Calculating thermal conductivity	7
f. Outline of the dissertation.....	8
II. Frequency Interference	8
a. Frequency Interference theory.....	9
b. Frequency Interference measurements	12
III. Thickness, Phase Change, and Detection of remote events.....	17
a. Thickness sensing at steady state	17
b. Lock-in response time.....	19
c. Real time monitoring of freezing and thawing water.....	21
d. Monitoring frozen and thawed mouse liver	24
e. Transient response to a distant event	27
IV. Front tracking.....	30
a. Experimental Setup.....	31
b. Calculating front position from raw 3ω data.....	33
c. Heater half width producing the same temperature rise as wire heater of fixed radius.....	36
d. Data processing and results	37
V. Conclusions and outlook.....	40
References	42

List of Figures

- Figure 1: Measurement of α TCR for a microfabricated gold heater line on a soda-lime glass substrate. a) Wire resistance as a function of temperature and input power. Dashed lines are linear fits for the data points. b) Cold wire resistance as function of temperature, using intercepts from fitted lines in a. The slope of this plot is $R_0\alpha$ TCR. 3
- Figure 2: 3ω sensors in various traditional configurations. a) Diagram of a 3ω strip heater, with labeled dimensional variables. Thermal penetration depths (L_p) are shown in the cross sectional views of b, c and d. All cross sectional views show a cut made midway between the V+ and V- probes in the XY symmetry plane. b) Strip heater on sample. c) Supported 3ω technique, with dielectric layer placed in order to measure electrically conductive samples. Dashed line represents adiabatic interface for the boundary mismatch approximation, discussed in Section I.e. d) Wire sensor, immersed in sample for thermal conductivity measurement of the liquid sample. 4
- Figure 3: Simplified experimental schematic used for a traditional 3ω measurement..... 6
- Figure 4: Schematics of a generalized 3ω experimental setup with multiple excitation frequencies, using the lock in voltage outputs converted to current inputs to the sensor..... 9
- Figure 5: Interference points (shown as multiplicative frequency spacing, m) for differing numbers of excitation frequencies (N)..... 12
- Figure 6: Schematics of experimental setup used to verify frequency interference behavior. a) Schematic of instrumentation. In this setup 4 lock-in amplifier signals were combined, using a Zurich HF2 for all 4 channels. Voltage adding was also done with the Zurich HF2. b) YZ view of sensing wire in oil with dimensions labeled. c) XY view of the sensing wire in oil. 13
- Figure 7: Frequency Interference. a) Interference effects for 2 superimposed signals using the experimental setup of Figure 6, along with the effect of time constant (τ) on coefficient of variation. Peaks correspond to solution values of m for equation (16), listed in Table 2. The width of the peaks is found to be inversely proportional to τ , as expected. b) Interference peaks for 4 frequencies, as tested by an identical experimental setup. The expected interference points are shown by the dots, for both the without THD (solid points) and with THD (open points). With one exception, all of the experimental noise peaks correspond with expected interference points accounting for THD in the lock-in amplifier's signal generation. The one exception is $m = 3.827$ (starred point), which is explained by power line interference because $\omega_0 m^3 / 2\pi = 60\text{Hz}$ 15
- Figure 8: a) Frequency sweep of the out-of-phase 3ω voltage measured from an ice sample with two different backside boundary conditions. The penetration depth for $500\mu\text{m}$ ice is denoted (black line), as well the frequency corresponding to $250\mu\text{m}$ ice (cyan line). Analytical solutions (lines) for isothermal and adiabatic sample backsides using known sensor and sample properties are shown for comparison. b) Frequency sweep for ice samples of fixed thickness of ($200\mu\text{m}, 500\mu\text{m}$), both with copper plates on the back side which approximates an isothermal boundary condition. Frequencies corresponding to $L_p = 500, 250, 200,$ and $100\mu\text{m}$ are marked with vertical lines. Analytical solutions for an isothermal sample backside using sensor and sample properties are shown for comparison (lines). 18
- Figure 9: Schematic for the multi-frequency 3ω measurements, using multiple lock-in amplifiers..... 19

Figure 10: Panel a) Time response of in-phase 3ω voltage to placement of room temperature water droplet. This corresponds to an increase in apparent thermal conductivity, as monitored by 3 simultaneously measured frequencies. Panel b) shows the same data sets with time normalized by lock in time constant, and in-phase 3ω voltage normalized by starting ($t = 0$) and ending (average from $t = 140$) voltages. The 3 curves exhibit similar behavior to the idealized RC circuit. 21

Figure 11: a) Real time monitoring of in-phase 3ω voltage during freezing and thawing test of water. b) Averaged in-phase voltages used for calculation of thermal conductivity (from panel a and Figure 10a). c) Corresponding thermal conductivity evolution over time, as calculated by the slope method (equation (6)) using in-phase 3ω voltage data collected during the experiment. d) Real time thermal conductivity as calculated from the out-of-phase 3ω voltage for each frequency (equation (6)). In panel d the thermal conductivity of the sensor (1.32 W/m-K), as measured from the in-phase data, has been subtracted. 22

Figure 12: a) Real time monitoring of in-phase 3ω voltage during freezing and thawing test of mouse liver. b) Averaged in-phase voltages used for calculation of thermal conductivity (from panel a). c) The corresponding thermal conductivity evolution over time, as calculated by the slope method (equation (6)) using in-phase 3ω voltage data collected during the experiment from the . d) The real time thermal conductivity as calculated from the out-of-phase 3ω voltage for each frequency (equation (5)). In panel d the thermal conductivity of the sensor (1.28 W/m-K), as measured from the in-phase data, has been subtracted. 26

Figure 13: Thermal response to a remote event: placement of a water droplet on frozen agar gel (effectively equivalent to an ice layer, as indicated in the schematic) in contact with the heater line. a) Real time monitoring of in-phase 3ω voltage during the remote event. b) Averaged in-phase 3ω voltages used for calculation of thermal conductivity (from panel a). Corresponding thermal conductivity evolution over time, as calculated by the slope method using in-phase 3ω voltage data collected during the experiment. d) Real time thermal conductivity as calculated from the out-of-phase 3ω voltage for each frequency. In panel d the thermal conductivity of the sensor, as measured from the in-phase data in Figure 10 and Figure 11, has been subtracted... 28

Figure 14: Principle of the front tracking measurement. Thermal penetration depths (purple, red) surrounding a heating wire (gold circle, long in the direction out of the page) embedded in two semi-infinite media (1, 2), with $\alpha_1 > \alpha_2$. In both panels, the L_{p2} is sensitive only to α_1 . In a), L_{p1} senses an effective thermal diffusivity that combines both α_1 and α_2 , whereas in b) L_{p1} is sensitive only to α_1 30

Figure 15: Schematics of experimental setup. a) YZ view of sensing wire in oil with dimensions labeled. b) Corresponding XY view, and camera seeing both the reflection of the wire and the wire itself. c) Schematic of instrumentation. In this setup 4 lock-in amplifier signals were combined, using a Zurich HF2 for 3 channels and an SRS830 lock-in amplifier for the 4th. Voltage adding was done with the Zurich HF2..... 31

Figure 16: Schematic of the cases compared in dimensionless groups defined in equations (20) and (21). 33

Figure 17: Comparison between in-phase (a) and out-of-phase (b) relationships between normalized depth and normalized 3ω voltage as defined in equations (20) and (21). Simulations are for a strip heater with $5\mu\text{m}$ half width. A line at $V_{3\omega} = 1$ is shown for aid in interpretation..... 34

Figure 18: Relationship between normalized depth and normalized voltage as defined in equations (20) and (21). Simulation configurations for a strip heater with $11.2\mu\text{m}$ half width (a),b)) and $5\mu\text{m}$ radius cylindrical heater c) are shown on their respective plots and are all infinitely long in the direction out of the page. a) Analytically calculated relationship for a line heater in an oil bath with an adiabatic boundary condition to approximate the surrounding air. b) Line heater analytical result with the finite thermal conductivity of air taken into account. Both a) and b) assume no convection occurs, and use the BMA. c) Results of a 2D FEM simulation of cylindrical heater immersed in oil, as well as simulation results from the 1 Hz line heater analytical solution (from b)). d) Error between the FEM simulations for the cylindrical heater and the line heater analytical solution, i.e. the difference between points and line in c)..... 35

Figure 19: Transient front tracking: determination of front position from out-of-phase 3ω voltage. a) Moving average filtered 0.147 Hz data to be converted into a position measurement; see text). b) Extraction at a rate of 383 nm/s. c) Infusion at a rate of 376 nm/s. d) Extraction at a rate of 95.1 nm/s. e) All 3 trials plotted together, on the axis of position as calculated from 3ω signals versus position as seen by camera. Color corresponds to frequency, as in previous plots, and different trials are plotted with different line styles. 39

List of Tables

Table 1: Settling time for different lock-in amplifiers as a function of roll-off setting.....	6
Table 2: Values of m solving equation (16) for $N = 2$ and $\Delta\omega = 0$, listed by ijk . Note i, j and k are interchangeable in equation (16).	14
Table 3: Penetration depths for measured electrical excitation frequencies, as defined in equation (4) .	21
Table 4: Summary of thermal conductivities extracted from water freezing and thawing data in Figure 11.	23
Table 5: Summary of thermal conductivities extracted from mouse liver freezing data from Figure 12. .	26
Table 6: Summary of calculated thermal conductivities before and after a remote event	28
Table 7: Thermal penetration depths for input current frequencies ($\omega/2\pi$) used in position tracking experiments	32
Table 8: Summary of 3 position tracking trials	38

Acknowledgements

In my PhD seminar I made the joke “I believe the expression is: it takes a village to make a PhD”. Though it was a joke, I firmly believe it to be true. I am grateful for the many amazing people who surround me in my life, and have supported me through graduate school.

In my time at Berkeley I have been a part of several great communities. This has come in many forms, such as groups I have swam with (Fuego and the Cal men’s swimming team), a meditation group at the Berkeley Shambhala center, and the labmates I have worked with. Each of these communities has accepted me for who I am, and given me opportunity to learn and grow. I am so grateful for the people that have made up these groups. In particular, thank you to my labmates. It had been great to work with so many smart, talented, and kind people. I will cherish the memories of working with you all.

I would like to specially thank the 2 people I would consider my primary mentors during my time in Berkeley. Dave Durden has, for reasons I may never entirely understand, allowed me to be a part of the training group with the Cal men’s swimming team for almost 5 years. I have matured immensely as a swimmer and as a person by being a part of this group of men. They have brought joy to my days, by making me laugh too many times to count. They have brought inspiration to my life as I see the way these men pursue greatness. Thank you Dave for allowing me to roll with you all, and for teaching me to be a better man along the way.

My academic mentor and advisor, Chris Dames, has taught me so much. Every interaction I learn something new, scientific or otherwise. Chris is one of the most kind and patient people I have ever known, and it never ceases to amaze me that he manages to find teachable moments in every interaction, despite his insanely busy schedule. It is hard to find the words to adequately express gratitude to someone who has mentored me professionally for 5+ years, but perhaps I can start by saying that working with Chris has been a joy. I cannot think of an experience that could better set me up for professional success.

Most importantly, I thank my family. My parents and brothers make up an unbelievable support network as I go through my life. None of this would have been possible if not for them.

I. Introduction

The study of heat transfer and thermodynamics allows insight into many phenomena in the world around us. Thermal physics helps us understand why water boils or freezes, why sweating cools our core body temperature and how the sun warms the earth, counteracting the second law of thermodynamics and allowing life to exist. Once one has even basic understanding of conduction, convection, and radiation, one starts to notice these phenomena around them constantly. The study of these phenomena is crucial in many fields and technologies.

This thesis focuses on one application of heat conduction. At the macroscopic scales, Fourier's law

$$q = -k \partial T / \partial x, \quad (1)$$

tells us that the heat flow in one direction through an object will be proportional to the temperature gradient in the object, with a proportionality constant. This constant is called thermal conductivity, k , and represents the ability of a material to conduct thermal energy. Knowledge of thermal conductivity of materials is important in any situation in which thermal management is a concern. These applications range in scale from insulation of residential buildings (to control indoor environments) to electronics cooling (to prevent hardware from overheating).

As knowledge of thermal conductivity is important in many real systems, many techniques have been developed to measure it. The cut bar method takes temperature measurements to extract thermal conductivity using the equation that defines it, equation (1). But not all materials are amenable to bulk measurements requiring a rigid sample. For systems of differing properties or geometries, other techniques have been developed such as the transient plane source technique [1] and various techniques based on thermorefectance [2] [3]. Each measurement technique has its own applications and systems for which it is optimal. One such technique is examined extensively in this thesis: the so-called "3 ω " technique (introduced later in this chapter).

Most thermal conductivity measurement techniques utilize samples of known geometries and boundary conditions [4] [1] [2] [3] to measure thermal properties. In this thesis, known thermal properties of materials are used to measure geometric properties of the system, changing the some of the typical inputs and outputs for thermal conductivity measurements. This workflow is somewhat analogous to the analytical approach of the inverse heat conduction problem, in which a typically known quantity (heat flux) is used to find a typically unknown quality (temperature). This is done with the objective of offering a solution to problems more often encountered in physical systems [5]. Examples of previous work to measure physical geometry using known thermal properties include using contrast in thermal properties of soil and landmines to detect the presence of buried explosives [6], or nondestructive defect testing through the contrast between fully dense solids and air gaps [7] [8]. Thermal property changes also frequently accompany phase change events, as in solidification of materials [9], and tissue during cryosurgery [10]. In the above examples, measurement of thermal properties in real time yields information about spatial location of regions with distinct thermal properties.

This thesis focuses on measurements occurring in transient systems, as would happen during cryosurgery. In a cryogenic treatment option for atrial fibrillation, the goal of surgery is to freeze entirely through the pulmonary vein to form scar tissue, while minimizing damage to surrounding tissue. This can lead to complications such as phrenic nerve palsy [11]. Pulmonary veins have a wall thickness of 1-2mm thick, and clinically available imaging techniques cannot provide an accurate measurement of ice formation in this scale. The surgeries are typically done without ability to accurately measure the ice formation. The 3ω technique can provide thickness measurements at this scale, as this thesis will demonstrate. Additionally, 3ω sensors can be integrated into surgical equipment already in use for this procedure, as demonstrated by Natesan et al. [12]. This allows for accurate measurements of ice thickness to occur during the surgery, decreasing probability of negative outcomes.

The rest of this chapter explains the 3ω method, and describes the conventional implementations for measuring thermal properties. As 3ω is fundamentally a resistance thermometry technique, the working principles of resistance thermometry will be detailed in the following section. Description of sensor, the electronics used to obtain measurements, and calculation of thermal conductivities will follow. This chapter ends with an outline of the original work that will be presented in the rest of this thesis.

a. Resistance thermometry

Over a large range of temperatures, metals have an electrical resistance which varies linearly with temperature change, often expressed as

$$R(T) = R(T_0)(1 + \alpha_{TCR}\Delta T), \quad (2)$$

where α_{TCR} , the temperature coefficient of resistance, is defined as

$$\alpha_{TCR} = \frac{1}{R_0} \frac{dR}{dT}. \quad (3)$$

In this relationship, R_0 represents the electrical resistance in the limit of no current at the temperature for which α_{TCR} is being defined. In these equations, T represents temperature, and T_0 is a reference temperature at which $R(T_0)$ is defined.

Knowledge of α_{TCR} and resistance at a specified temperature ($R(T_0)$) mean that by measuring the electrical resistance, the temperature of the metal can be easily calculated. In bulk metals, α_{TCR} is well documented. In microfabricated metals, α_{TCR} may differ significantly from that of bulk samples, due to increased defects, grain boundaries, and film surfaces [13]. In this case, α_{TCR} can be directly measured (Figure 1). This is done by measuring voltage across a resistor at a variety of currents. Taking the slope of the linear relationship between resistance versus power at each temperature, the resistance at zero input current (cold wire resistance, R_0) can be calculated for each temperature (Figure 1a). The slope of these intercepts of cold wire resistance as a function of temperature is $R_0\alpha_{TCR}$ (Figure 1b). The measurement in Figure 1 is done with a gold heater line (width $2b = 80\mu\text{m}$, length $L = 1.5\text{mm}$, thickness $t = 200\text{nm}$) evaporated onto a soda-lime glass substrate.

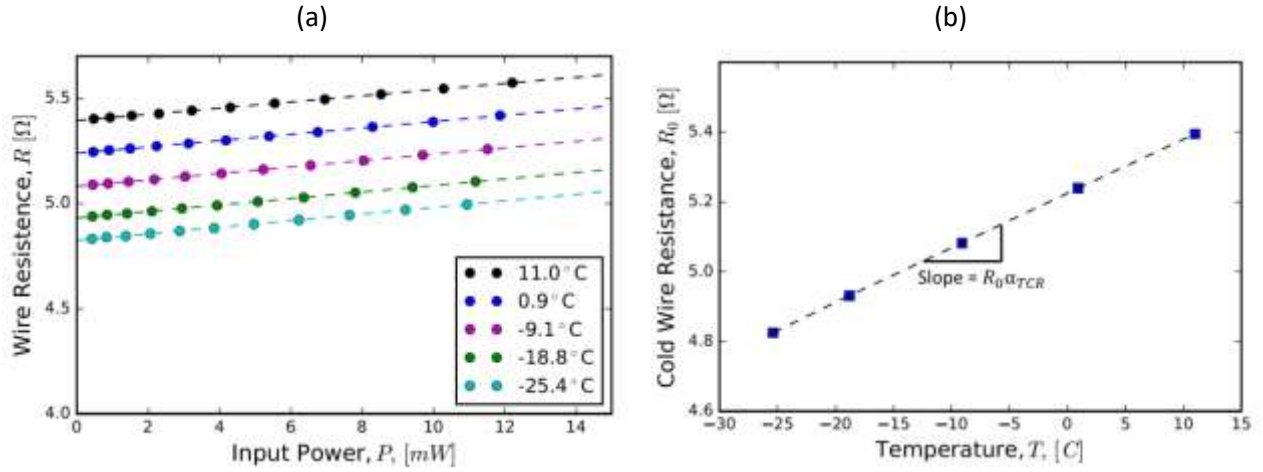


Figure 1: Measurement of α_{TCR} for a microfabricated gold heater line on a soda-lime glass substrate. a) Wire resistance as a function of temperature and input power. Dashed lines are linear fits for the data points. b) Cold wire resistance as function of temperature, using intercepts from fitted lines in a. The slope of this plot is $R_0\alpha_{TCR}$.

b. 3ω measurements

The 3ω technique uses resistance thermometry to measure thermal conductivity of a sample. It has been used for measuring the thermal conductivity of solids [4], liquids [14], and gases [15]. In this technique, a microfabricated strip heater (Figure 2a and b shows typical geometry) or heating wire (Figure 2d) is used. Key in the analysis of this technique is the approximation of the heater as a line source. There is one geometrical condition for this approximation, that the heater line length in the z direction must be large compared to the width of the heater line, $L \gg b$, where L is heater line length in the z direction, and b is the heater line half width in the x direction (see Figure 2). The term “heater line” will be used in this thesis as shorthand meaning a heater of either the strip or wire type.

Additionally, the analysis of the technique assumes the heater line can be approximated as a point source in the XY direction. This is tested by the comparing width of the heater line to the thermal penetration depth. Thermal penetration depth is a central concept in this thesis, and is defined as

$$L_p = \sqrt{\frac{\alpha}{2\omega}}, \quad (4)$$

where α is thermal diffusivity, ω is excitation frequency (units of radians per second) and the factor of 2 is due to the joule heating occurring at twice the electrical excitation frequency. Thermal penetration depth represents the length scale over which heat diffuses into the sample. The heater line can be approximated as a point source with less than 1% error if $L_p/b > 5$ [16]. The final assumption related to

heater line geometry is that the heater line appears infinitely long thermally, so complications due to heat flow towards the ends of the line can be neglected. This is expressed as $L/L_p \geq 4.7$, for less than

1% error in the calculation of thermal conductivity [17], assuming separate voltage and current pads, as shown in Figure 2a.

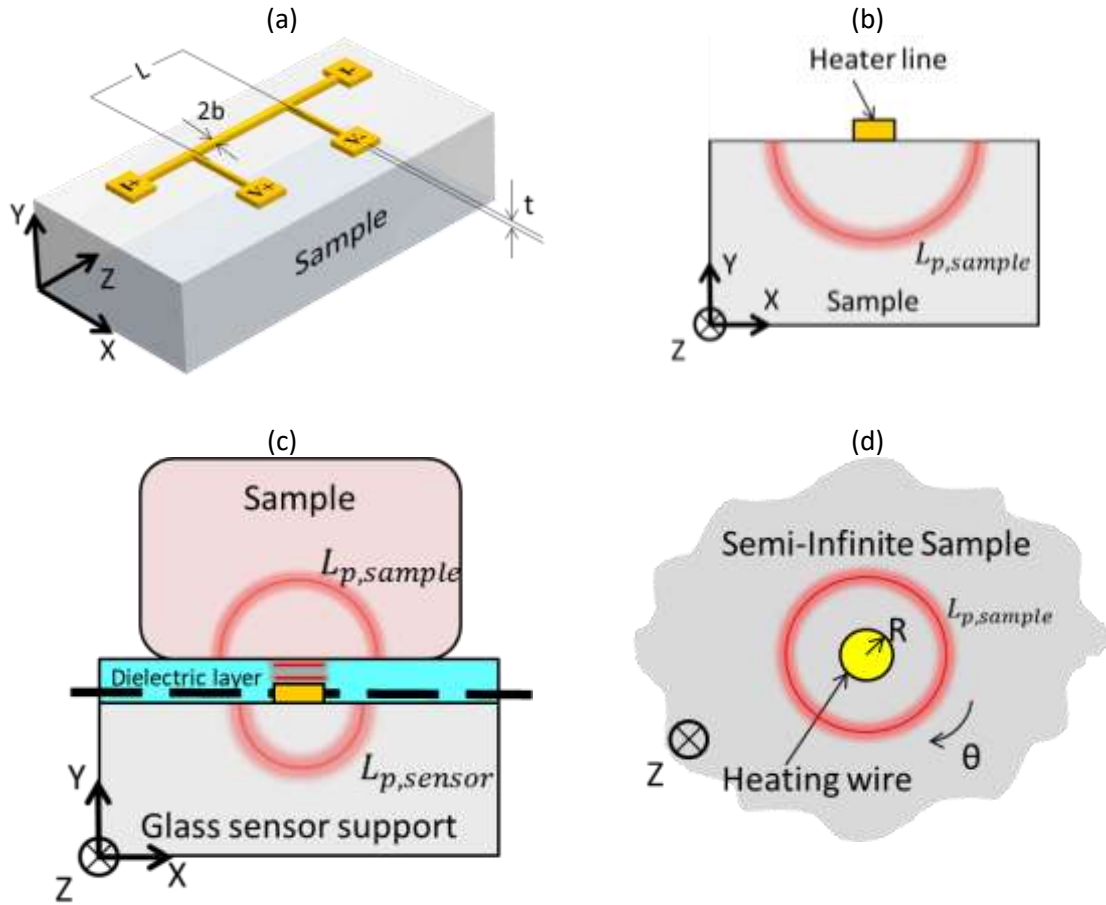


Figure 2: 3ω sensors in various traditional configurations. a) Diagram of a 3ω strip heater, with labeled dimensional variables. Thermal penetration depths (L_p) are shown in the cross sectional views of b, c and d. All cross sectional views show a cut made midway between the V+ and V- probes in the XY symmetry plane. b) Strip heater on sample. c) Supported 3ω technique, with dielectric layer placed in order to measure electrically conductive samples. Dashed line represents adiabatic interface for the boundary mismatch approximation, discussed in Section I.e. d) Wire sensor, immersed in sample for thermal conductivity measurement of the liquid sample.

In a 3ω measurement, the heater line is excited at a current with frequency ω . This excitation creates joule heating in the heater line, given by $Q = R_0 I^2$. Squaring the alternating current signal leads to a heating at the second harmonic (2ω). Because the resistance of the heater line is proportional to its temperature, the Joule heating will create a resistance fluctuation with frequency 2ω . The interaction of the 1ω current and 2ω resistance creates a 1ω and 3ω voltage. These can be measured directly. The 3ω voltage varies based on the thermal conductivity (k) and heat capacity (ρc) of the material stack in contact with the heater line. All sensor configurations in Figure 2 have the same operating principle, exciting the heater line with an alternating current at frequency ω , and measuring the resulting 3ω voltage. Figure 2 shows 3 different physical setups to measure 3ω voltages, which will be discussed in greater detail in Section I.e, where the data analysis is described.

c. Lock-in amplifier

The voltage signals in a 3ω measurement take the form of time-varying periodic signals with noise. This signal can be expressed as a magnitude and phase at a given frequency. The measurements of these components are typically taken with a lock-in amplifier, which is functionally equivalent to a highly tunable band-pass filter in series with an amplifier. The purpose of this is to reduce the signal down to an in-phase and out-of-phase component, while filtering out any signal that is not at the frequency of the thermal response to the excitation signal. The details of the lock-in amplifier operation will become important in the subsequent chapters.

A lock in amplifier multiplies the time-varying periodic signal by a reference signal of known frequency. This multiplication will convert all periodic voltages of form $\cos(\omega t)$ into signals of the form $\cos(\omega t \pm \omega_{ref} t)$. If an input signal is the same frequency as the reference signal, it will be converted into a DC and 2ω component. The lock-in amplifier then uses a low pass filter to remove the 2ω component, and measures the DC signal. This DC signal represents the in-phase signal, and a second multiplication by a 90° phase offset reference signal yields the out-of-phase [18]. These are also referred to as the X and Y components of the signal, respectively, or can be converted into an equivalent magnitude and phase. Signals of any other frequency are considered measurement noise. The noise signals are filtered out using the low pass filter. The low pass filter's RC time constant can be set on the lock-in amplifier, and controls the passband of the filter. Changing the passband represents a tradeoff between response time and noise filtering. A larger time constant (smaller passband) will yield greater filtering of noise signals with longer response time, while a smaller time constant (larger passband) will filter comparatively less noise with a faster response time. This response time is further modulated by the order of the RC filter, with higher filters orders providing better noise suppression, at the cost of increasing settling time.

Settling time can be defined here as the time taken for the measured signal to be within an error band of 1% in response to a step change in the system being measured. Settling time will depend on both the lock in time constant, and the roll off setting, which determines the roll off of the low pass filter. This is done by placing multiple low pass filters in series, and activating the number desired. For example, in the in the case of a SRS830 and Zurich HF2MF lock-in amplifiers, the information in

Table 1 is provided. Each low pass filter has an individual roll-off of 6 dB/octave, and the roll off increases by 6 dB/octave for each filter activated. As with time constant, increasing the filter order will provide a less noisy signal, but at the expense of filter response time.

Table 1: Settling time for different lock-in amplifiers as a function of roll-off setting

Roll off setting [dB/Oct]	Settling time to 99% [number of lock-in time constants]	
	SRS830 [18]	Zurich HF2MF [19]
6	5	4.6
12	7	6.6
18	9	8.4
24	10	10

30	[N/a]	12
36	[N/a]	12
42	[N/a]	15
48	[N/a]	16

d. Experimental setup

A typical schematic of a 3ω experimental setup is shown in Figure 3. The lock in amplifiers used in this thesis (SRS 830, Zurich HF2) have voltage output capability, so a V-to-I conversion circuit is used to convert the voltage output to a current input for the heater line. The heater line is in contact with the sample to be measured, as shown in Figure 2.

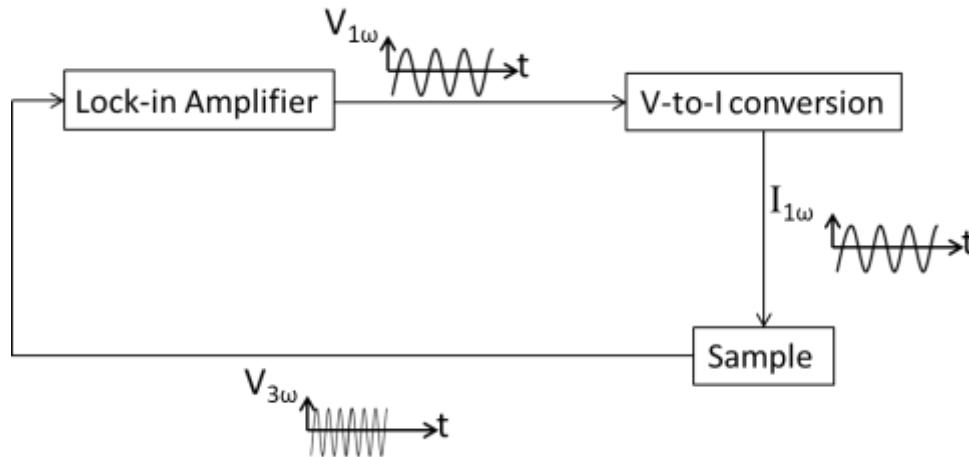


Figure 3: Simplified experimental schematic used for a traditional 3ω measurement.

The time varying third harmonic voltage ($V_{3\omega}$) can be expressed as either magnitude (R) and phase (θ), or as an in-phase ($V_{3\omega,IP}$) and out-of-phase ($V_{3\omega,OP}$) component. All of these quantities are measurable by the lock-in amplifier.

e. Calculating thermal conductivity

The measurement configuration of Figure 2a and b (referred to in this thesis as “traditional 3ω ”) has been studied extensively [4] [16] [20] [17] [21], representing a technique that can measure the thermal conductivity of a rigid, electrically insulating solid after evaporating a heater line onto it. In this type of measurement the in-phase and out-of-phase component of third harmonic voltage are collected by the lock-in amplifier. Either component of the voltage can be used to calculate a sample’s thermal conductivity. In the case of a strip heater, it is readily shown from the equations in [20] that the out-of-phase data yields a relationship

$$k = \frac{\alpha_{TCR} R^2 I^3}{8LV_{3\omega,OP}}, \quad (5)$$

relating the out-of-phase 3ω voltage with the thermal conductivity of the sample. In this equation, I is RMS input current. The in-phase 3ω voltage can also be used to calculate thermal conductivity, using

$$k = \frac{\alpha_{TCR} R^2 I^3}{4\pi L \frac{dV_{3\omega,IP}}{d \ln f}} \quad (6)$$

The equations presented for thermal conductivity are valid when the heating from the heater line is well-contained within the sample being measured. In order to be sensitive to only the thermal properties of the sample, L_p should be well within the sample, ideally with $L_p/h \leq 1/2$, where h is thickness of the sample in the y direction [17].

To extend this measurement technique beyond the measurements of electrically insulating solids that are amenable to direct microfabrication of a heating line, the so called “supported” 3ω technique (Figure 2c) is used. In this implementation of the technique, a heater line is fabricated on a support (often glass), and the sample is placed directly on top of the sensor/support combination. This allows for non-rigid and/or electrically conductive samples such as biological tissue or liquids to be measured [22] [23] [24] [25]. In the supported technique, there is a dielectric layer placed over the heater line, so electrically conductive samples can be measured. If the dielectric layer is thin compared to the thermal penetration depth, the heat flow through the dielectric layer is approximately 1 dimensional, as shown in Figure 2c.

To analyze data collected with the supported 3ω technique, the boundary mismatch approximation (BMA) is applied [22]. This assumes that the heat flows into the sensor and sample separately, with the heat flow in each direction assumed to be determined by the ratio of thermal impedances of materials above and below the heater line. Stated alternately, it is assumed that no heat will cross the dashed line in Figure 2c, and the heat flow in each direction will be determined by the thermal properties on either side of the dashed line. In this case, the sensor and sample are treated as parallel thermal impedances and the measured thermal conductivity will simply be a sum of the sensor and sample

$$k_{measured} = k_{sensor} + k_{sample} \quad (7)$$

Lubner et al. [26] gives a detailed analysis of the broad thermal property range in which this approximation is valid.

Figure 2d shows a third implementation of the 3ω technique, with a different sensor geometry, used for probing the thermal conductivity of liquids [22] [15]. As long as the liquid is of sufficient thickness (greater than $2L_p$), the measurement will only be sensitive to the thermal properties of the fluid sample. This uses a cylindrical wire as the heater line to measure the thermal conductivity of the liquid sample the heater line is in contact with. In this thesis, the supported 3ω technique of Figure 2c is used in Chapter III, and a configuration similar to Figure 2d is used in Chapters II and IV.

f. Outline of the dissertation

Following this introductory chapter, this document is broken up into 4 chapters. These chapters detail the progress towards using the 3ω technique to track moving interfaces in real time.

Chapter II details analytical and experimental work done to understand the complications arising from introducing multiple excitation frequencies into the 3ω system. An analytical understanding is developed, and verified through experiments.

Chapter III details experiments that verify the ability of the 3ω technique to sense step changes in thermal properties in real time. This is tested through transient measurements of water droplets placed on supported sensors, phase change events, and response to changes in thermal properties occurring away from the heater line. Along with verification that the technique can measure transient changes in thermal properties, the results are analyzed to extract thermal conductivities from both in-phase and out-of-phase 3ω voltages

Chapter IV details an experimental setup designed to use 3ω voltages to measure the transient position of a moving interface, as well as the modeling to support the experimental work. The experiment uses a Wollaston wire sensor and measures the 3ω voltages as an oil-air interface moves towards and away from the wire sensor. Numerical modeling is done to convert the measured voltages into positions, and these measurements are compared to camera images.

Chapter V provides a summary of the thesis, and a brief outlook on future directions.

II. Frequency Interference

Monitoring the voltage response to multiple excitation frequencies simultaneously can increase the speed at which a 3ω frequency sweep can be done, enabling multiple penetration depths to be probed simultaneously. The approach of multiple excitations is of particular interest when it is desirable to measure changes in thermal properties in real time. Probing at multiple excitation frequencies can be used to simultaneously gain information about multiple spatial regions in the sample (since each frequency has a different thermal penetration depth), as well as to use information from multiple channels to cross-check the measurement. In any of the cases above, it is crucial to understand how multiple excitations will interact to create the 3ω voltage signals that will be measured, in order to get accurate measurements.

The generalized schematic of such an experiment (using lock in voltage outputs converted to current excitations) is shown in Figure 4. For the generalized case of N lock in channels which generate N excitation signals and monitor N third harmonic signals, the frequency interference condition is derived below.

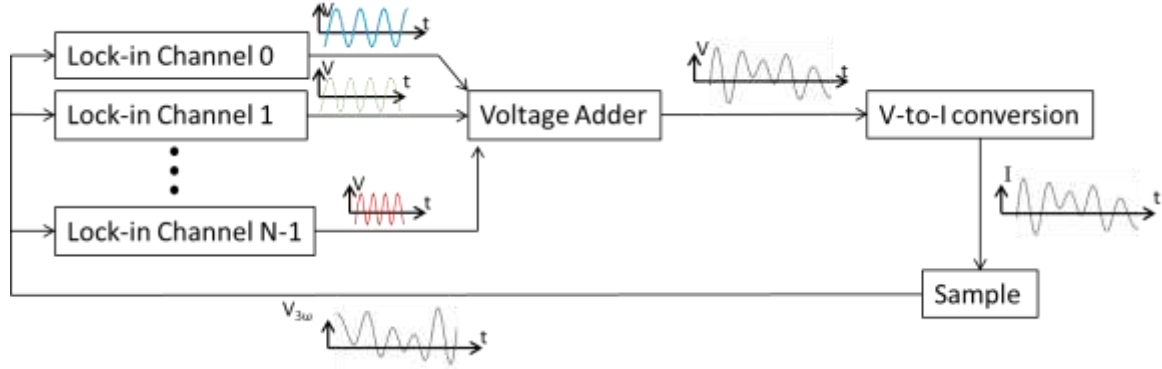


Figure 4: Schematics of a generalized 3ω experimental setup with multiple excitation frequencies, using the lock in voltage outputs converted to current inputs to the sensor.

a. Frequency Interference theory

For excitation by a single frequency, the classic 3ω equations [1] [16] explain the interactions of the various signals in the electrical and thermal domains. Here the analysis is generalized for simultaneous excitation by multiple frequencies. To become oriented to the combinatorial character of the problem, first note that driving the sensor with superposed sinusoidal currents at N frequencies creates N^2 joule heating signals. Because of the linearity of response in the thermal domain, these N^2 heat sources cause N^2 temperature responses, and thus N^2 frequency signals in the resistance of the sensor due to its temperature coefficient of resistance [1] [16]. Finally, applying Ohm's law to this superposition shows that each of the N current excitation frequencies multiplies each of the N^2 resistance perturbations to yield N^3 voltage responses. Among these N^3 signals, only N are the desired third harmonic signals which are used to analyze this experiment as N independent implementations of the classic 3ω method, while the other $(N^3 - N)$ signals can be thought of as noise which may corrupt desired signals.

To ensure that none of the $(N^3 - N)$ "noise" signals fall at a frequency close to any of the N targeted third harmonic signals, the frequency mixings are analyzed further building on the methods of [16]. Consider N arbitrarily spaced frequencies $\omega = \{\omega_0, \omega_1 \dots \omega_{N-1}\}$. Following the standard 3ω equations, the i -th excitation ω_i causes a voltage at $3\omega_i$ which is directly proportional to the system's thermal response (thermal transfer function) at $2\omega_i$ [16]. However, because we are superposing multiple excitation frequencies, the multiplication of these many signals in the electrical and thermal domains opens up the possibility for other signal mixings to also cause a voltage at $3\omega_i$ which may be completely unrelated to the thermal response of interest and thus confuse the analysis.

Here, all individual excitations are taken for simplicity to have the same unity amplitude. First consider these N frequencies all to be separated by the same multiple, m , anchored from a baseline reference signal at an angular frequency ω_0 . Thus in the time domain the excitation can be written,

$$I_{TOT}(t) = I_0 + I_1 + \dots + I_{N-1} = \sin(\omega_0 t) + \sin(m\omega_0 t) + \sin(m^2\omega_0 t) + \dots + \sin(m^{N-1}\omega_0 t) = \sum_{i=0}^{N-1} \sin(\omega_0 m^i t). \quad (8)$$

Joule heating of the wire is given by [16]

$$Q(t) = I^2(t)R_0, \quad (9)$$

with R_0 defined as the resistance of the sensor in the limit of zero current. Thus

$$Q(t) = R_0[\sin(\omega_0 t) + \sin(m\omega_0 t) + \sin(m^2\omega_0 t) + \dots + \sin(m^{N-1}\omega_0 t)]^2. \quad (10)$$

The heating frequencies are

$$\omega_{heating} = (\pm(m^i) \pm (m^j))\omega_0 \quad \text{where } i, j = 0, 1, 2 \dots N - 1, \quad (11)$$

which also are the frequencies of the resulting temperature responses, because of the linearity of the system in the thermal domain (the heat diffusion equation with constant properties). Furthermore, since the resistance of a metal line will change in direct proportion to the (small) temperature changes, the electrical resistance R will also have small oscillations at the frequencies $\omega_{heating}$, as listed in equation (11)

From Ohm's law these current and resistance signals will combine to create voltage signals,

$$V = IR \propto [\sin(\omega_0 t) + \sin(m\omega_0 t) + \dots + \sin(m^{N-1}\omega_0 t)] \times [\sin(\omega_0 t) + \sin(m\omega_0 t) + \dots + \sin(m^{N-1}\omega_0 t)]^2. \quad (12)$$

This equation neglects the DC portion of the signal, which is not important in this analysis. These voltage signals will have frequencies of

$$\omega_{voltages} = (\pm(m^i) \pm (m^j) \pm (m^k))\omega_0, \quad \text{where } i, j, k = 0, 1, 2 \dots N - 1. \quad (13)$$

These signals contain a wealth of information about the system's thermal response at the joule heating frequencies, i.e., $Z(\omega_{heating})$ where Z is the thermal transfer function [16]. However, the extensive mixing of frequencies greatly complicates the interpretation. Here we focus on the simplest case which corresponds to a decoupled superposition of the single-frequency classical 3ω analysis, that is, a one-to-one mapping between $V(\omega_{monitor})$ and $Z(\frac{2}{3}\omega_{monitor})$, where $\omega_{monitor}$ is a monitored frequency and the factor of $\frac{2}{3}$ is derived in [16]. In this case we monitor N channels each of which corresponds to the 3rd harmonic of one of the excitation sinusoids. That is, the desired voltage signals occur at

$$\omega_{monitor} = \pm 3m^l, \text{ where } l = 0, 1, 2 \dots N - 1. \quad (14)$$

We require these $\omega_{monitor}$ frequencies to be independent of all the other frequencies enumerated in the $\omega_{voltages}$ list above (equation (13)), for otherwise there would be cross-talk among multiple signals

which would invalidate the decoupled single-frequency classical 3ω analysis. Thus, undesired frequency interference will occur if

$$(\pm(m^i) \pm (m^j) \pm (m^k))\omega_0 = \pm 3(m^l)\omega_0. \quad (15)$$

Allowing for a finite frequency acceptance bandwidth $\Delta\omega$ of the lock-in amplifier detection, after simplification, the condition for interference becomes

$$|3(m^l) - |\pm(m^i) \pm (m^j) \pm (m^k)|| \leq \Delta\omega/\omega_0, \text{ where } i, j, k, l = 0, 1, 2 \dots N - 1. \quad (16)$$

Equation (16) is alternately expressed as

$$|\pm(m^i) \pm (m^j) \pm (m^k) \pm 3(m^l)| \leq \Delta\omega/\omega_0, \text{ where } i, j, k, l = 0, 1, 2 \dots N - 1. \quad (17)$$

Note that each \pm sign implies a pair of equations, so with four such signs this expression implies $2^4 = 16$ distinct inequalities. Of note, $i = j = k = l$, is the condition of the desired single-frequency 3ω signal.

Relaxing the requirement that the frequencies be equally spaced by the multiplier m , the above derivation can be generalized for N arbitrarily spaced frequencies, $\omega = \{\omega_0, \omega_1 \dots \omega_{N-1}\}$. The frequency-interference condition, equation (17), generalizes to

$$|\pm\omega_i \pm \omega_j \pm \omega_k \pm 3\omega_l| \leq \Delta\omega, \text{ where } i, j, k, l = 0, 1, 2 \dots N - 1. \quad (18)$$

The bandwidth $\Delta\omega$ is related to the lock-in settings [15] through

$$\Delta\omega = \frac{FO}{2\pi\tau}, \quad (19)$$

where τ is the time constant setting of the lock-in amplifier and FO is the filter order, determined by the roll off setting. This $\Delta\omega$ equation gives the -3dB point of the bandpass filter.

The values of m that satisfy equation (17) for each N of 2 through 8 were found numerically, and are shown below in Figure 5. The significance of this plot is that each point represents a value of m for which one of the measured 3ω voltage channels will experience corruption resulting from the cross-talk due to interaction of excitation frequencies. This is referred to as frequency interference in this thesis, and represents multiplicative differences in excitation frequencies that should be avoided if an individual, uncorrupted 3ω signal is desired. Notably, the region between $m=4.23$ and $m=5.00$ is clear of points, meaning that this window of multiplicative spacing will minimize observed interference, and should

require smaller lock-in time constants (corresponding to faster response times) to achieve the same signal-to-noise ratio.

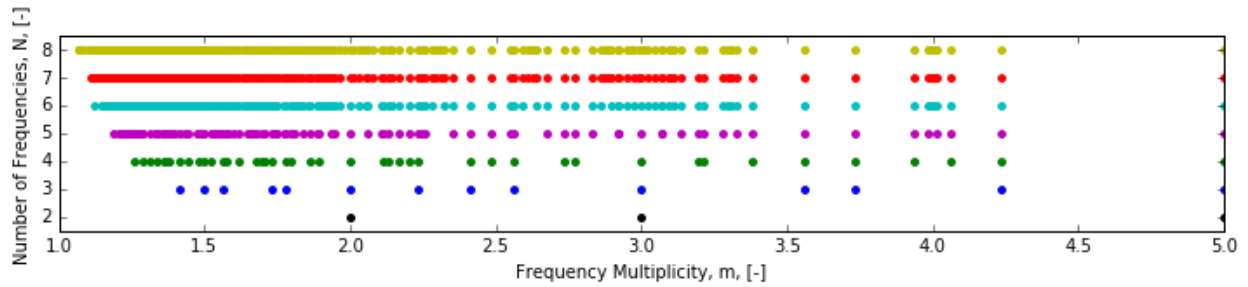


Figure 5: Interference points (shown as multiplicative frequency spacing, m) for differing numbers of excitation frequencies (N)

b. Frequency Interference measurements

The two frequency case ($N = 2$) and 4 frequency case ($N = 4$) were verified using the experimental setup shown in Figure 6 to test the interference points predicted by equation (17) above. This setup uses a platinum wire immersed in mineral oil (Sigma-Aldrich M8410) as the 3ω sensor and sample, respectively. Mineral oil was chosen as the sample for its dielectric nature. For these experiments d_{oil} , h_{wire} , and l_{sensor} were set to be large compared to the thermal penetration depths of all frequencies used, so the measurements will only be sensitive to the thermal properties of the mineral oil. Additional details on the construction of this setup are given in Section IV.b, as the design is more relevant to the experiments detailed there. A Zurich HF2 lock-in amplifier was used for all channels for both the 2 and 4 excitation frequency tests, as well as being used as the voltage adder.

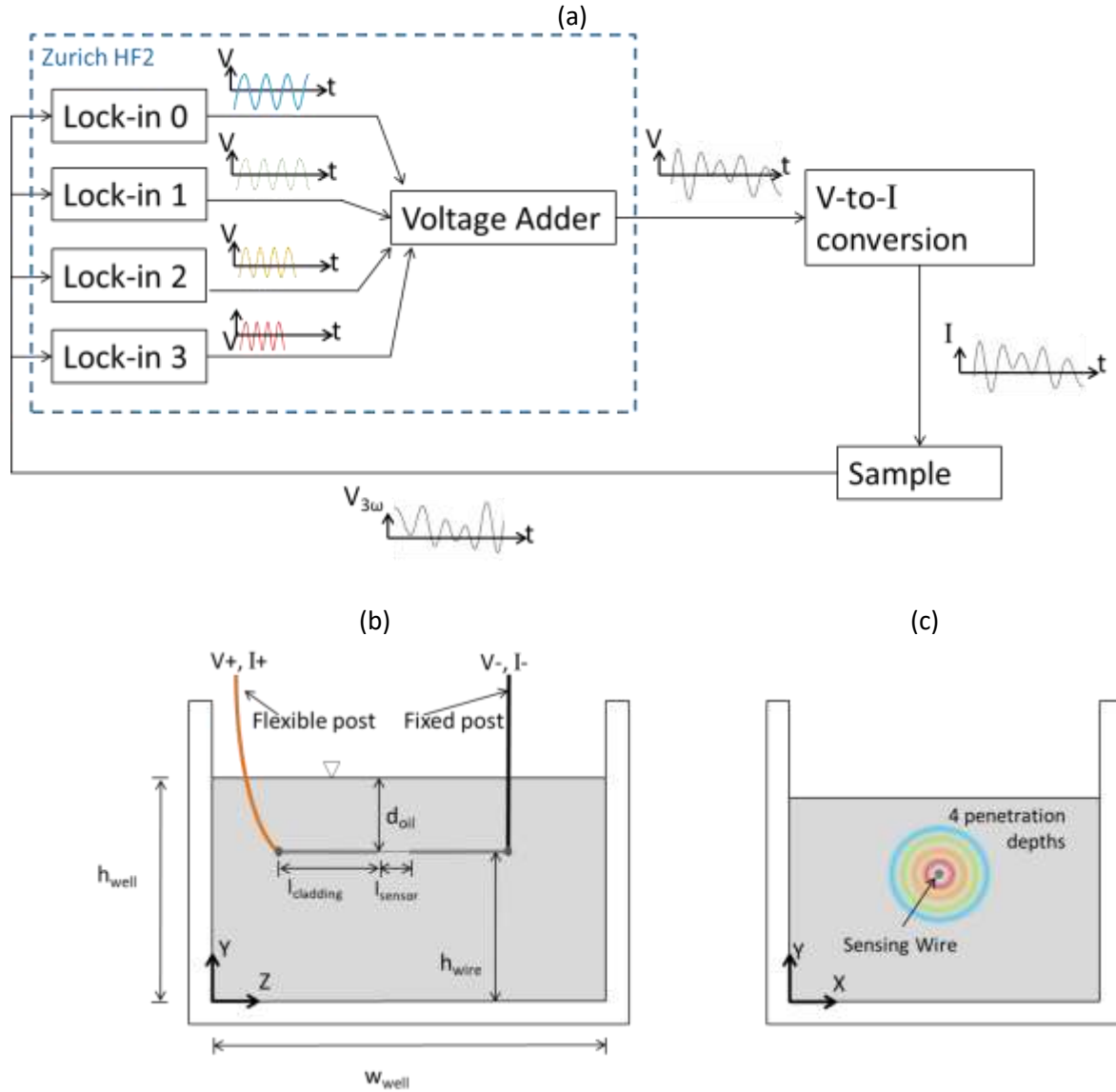


Figure 6: Schematics of experimental setup used to verify frequency interference behavior. a) Schematic of instrumentation. In this setup 4 lock-in amplifier signals were combined, using a Zurich HF2 for all 4 channels. Voltage adding was also done with the Zurich HF2. b) YZ view of sensing wire in oil with dimensions labeled. c) XY view of the sensing wire in oil.

These measurements were performed with the goal of identifying frequency multiplicities at which interference effects could be observed. Interference is observed here as increased noise in the signal, quantifiable by increased standard deviation of any measured 3ω voltage. Specifically, the coefficient of variation of the signal provides a relative measurement of how much noise is present in the pass band of the lock in amplifier,

$$COV \equiv \frac{\sigma}{\mu} = \frac{\text{standard deviation}}{\text{mean}} \quad (20)$$

This is one way to quantify the level of noise present in the signal.

By way of example, we considered equation (17) both mathematically and experimentally for the special case $N = 2$. Table 2 enumerates the 3 values of $m > 1$ which satisfy equation (17).

So for example, when $i=1, j=0, k=1, \text{ and } l=0$, two lock-ins are driven at frequencies $\{\omega_0, m\omega_0\}$. In this case, and using $\Delta\omega = 0$, equation (17) corresponds to

$$\pm(m^1) \pm (m^0) \pm (m^1) \pm 3(m^0) = 0.$$

Two solutions to this equation can be found for $m=2$, namely,

$$2 - 1 + 2 - 3 = 0 \quad \text{and} \quad -2 + 1 - 2 + 3 = 0,$$

as indicated in the fourth row Table 2. At the same time, for these $ijkl$ values there are no solutions for any other values of $m > 1$, as confirmed numerically.

Table 2: Values of m solving equation (17) for $N = 2$ and $\Delta\omega = 0$, listed by ijk . Note l, j and k are interchangeable in equation (17).

ijk	$l = 0$	$l = 1$
000	$m=1$ (original solution)	-
100,010,001	$m = 5$	-
011,101,110	$m = 2$	-
111	$m = 3$	$m = 2$

To confirm this predicted interference behavior experimentally, the frequency multiplicity m was varied, and the noise was measured via the maximum single channel COV among all in-phase and out-of-phase 3ω voltage signals. This COV is plotted below in Figure 7a for an $N=2$ channel experiment, in which each of i, j, k , and l can take values of 0 or 1. Each interference point is labeled with the corresponding $ijkl$ indices that describe which signals combined to create that point. In **Error! Reference source not found.a**, since $N = 2$, $ijkl$ can take values of 0 or 1. ω_0 was chosen to be 0.164 rad/s in this experiment.

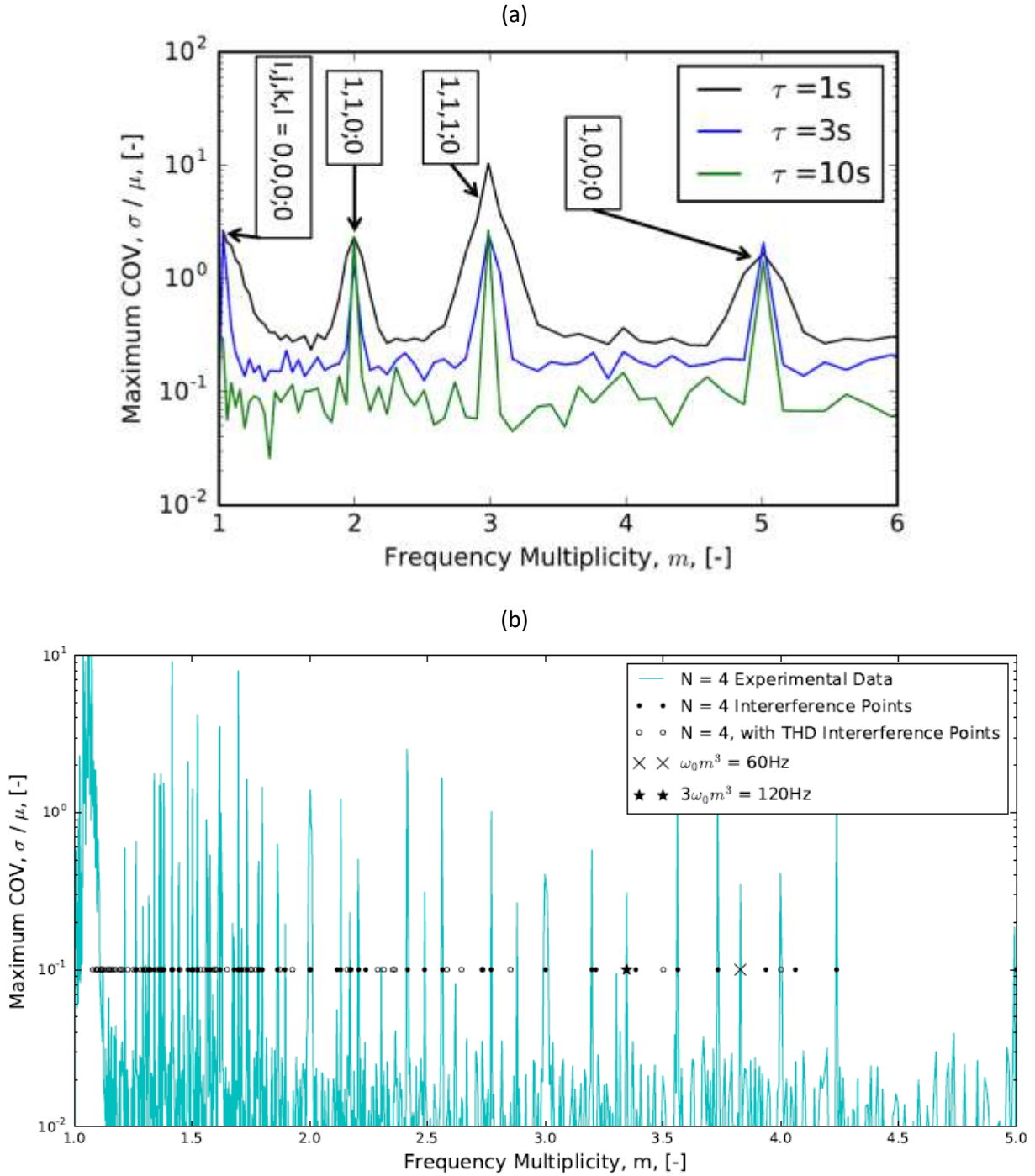


Figure 7: Frequency Interference. a) Interference effects for 2 superimposed signals using the experimental setup of Figure 6, along with the effect of time constant (τ) on coefficient of variation. Peaks correspond to solution values of m for equation (17), listed in Table 2. The width of the peaks is found to be inversely proportional to τ , as expected. b) Interference peaks for 4 frequencies, as tested by an identical experimental setup. The expected interference points are shown by the dots, for both the without THD (solid points) and with THD (open points). With two exceptions, all of the experimental noise peaks correspond with expected interference points accounting for THD in the lock-in amplifier's signal generation. The two exceptions are $m = 3.344$ (starred point) for which power line interference is expected as $3\omega_0 m^3 / 2\pi = 120\text{Hz}$, and $m = 3.827$ (starred point) which is explained by power line interference because $\omega_0 m^3 / 2\pi = 60\text{Hz}$.

Figure 12Figure 7**Error! Reference source not found.**a verifies the two frequency behavior, by showing that all solutions for m in the case that $N = 2$ (see Table 2) correspond to peaks in the figure. Specifically, m of 2, 3, and 5 correspond to regions around which the third harmonic signals will overlap with the passband of the sensing frequency. The passband (and therefore the width of each peak) is determined by the time constant setting of the lock-in amplifier, which is varied for 3 otherwise identical m sweeps to show that increasing time constant leads to a smaller lock-in passband, as expected. This illustrates the effect of the time constant on $\Delta\omega$, the affected frequency range around one desired signal. This can be mitigated by increasing the lock-in time constant, at the expense of response time [14] (this is verified experimentally in Section III.b. Since fast response time is desirable in any real-time tracking application, this approach should be applied with caution.

The 4 frequency test is shown in Figure 7**Error! Reference source not found.**b using a long time constant of 50 seconds to minimize peak size to be able to separate each distinct frequency interference location. In this case $N = 4$, so $i, j, k,$ and l can take values of 0, 1, 2, or 3. From numerically solving equation (17) for $N=4$, the expected interference conditions are indicated by the filled points (plotted arbitrarily at 0.1 on the COV axis, for convenience of visualization). Clearly not all experimental interferences are explained by the $N = 4$ case, see for example the strong experimental noise peak at $m=4$. This is attributed to total harmonic distortion (THD) effects in the voltage output from the lock-in amplifier. To support this, the interference analysis has been generalized by incorporating the second harmonic of each of the driving frequencies, i.e. generalizing the driving frequencies from $\frac{\omega}{\omega_0} = \{1, m, m^2, m^3\}$ to $\frac{\omega}{\omega_0} = \{1, m, m^2, m^3, 2, 2m, 2m^2, 2m^3\}$. The solutions of equation (17) for accounting for signals generated by THD effects in the lock-in amplifier are also plotted, as empty points. Now each measured interference point is a subset of the $N = 4$ with THD points, with two exceptions occurring at $m=3.344$ and $m=3.827$. The former corresponds to the monitored frequency being at 120 Hz, 3 times the line frequency, as ω_0 of 0.170 rad/s was used in these experiments. The latter corresponds to the highest excitation frequency being at 60 Hz. Based on Figure 7b, a frequency multiplicity of 4.78 was chosen for the position tracking experiments in Chapter IV, to minimize potential interference effects as well as span a large range of penetration depths.

The 2 plots of Figure 7 collectively support the model for predicting frequency interference, cumulating in equation (18), and for the special case of multiplicatively spaced excitation frequencies in equation (17). This gives a framework with which to design future experiments in which discerning individual 3ω voltage signals are desirable in a system with multiple excitations. Another potential avenue for gaining information is to ignore frequency interference effects during experiments, and use the understanding demonstrated in this thesis in data analysis to extract the desired information. It is conceivable to even design experiments to intentionally try to exploit interference effects to gain more information about the system. This is a potential direction for future work with this technique, but not one that is explored here.

III. Thickness, Phase Change, and Detection of remote events

This chapter demonstrates 2 primary results: the ability of the 3ω technique to sense thickness of a sample in contact with the heater line, and the ability of the 3ω technique to sense step changes in thermal properties when a frequency is monitored continuously. Both of these capabilities are needed in order to sense the position of a moving front (thickness sensing) in real time (response to a change in thermal properties). Each represents utilizing a measured third harmonic voltage in a way that is not typically done in the literature. The conceptual proof of these capabilities serves as a stepping stone upon which the results of Chapter IV are built. In addition, a measurement using multiple lock-in amplifiers is demonstrated, verifying the results of Chapter II. In this way, Chapter III serves as a bridge between the preceding and successive chapter's results.

a. Thickness sensing at steady state

In traditional 3ω measurements, it is desirable for the sample thickness to be large compared to the thermal penetration depth in order to only be sensitive to the thermal properties of the sample, as discussed in Chapter I. In order to sense layer thickness, the range of frequency operation should be in a different regime than either a traditional 3ω measurement or a thin film measurement. The thermal penetration depth should range from inside the layer to beyond it. To this end, if a frequency sweep is done corresponding to a penetration depth within the sample (high frequency) to well through the sample (low frequency), the measurement should become sensitive to the boundary condition on the backside of the sample for frequencies which the penetration depth extends through the sample (see diagrams in Figure 8a). This should cause a decrease in apparent thermal conductivity if the backside layer has a lower thermal conductivity than that of the sample, or an increase in apparent thermal conductivity if the backside has a higher thermal conductivity than the sample. This can be tested by using materials with high and low thermal conductivities (as compared to the sample) as the backside layer, representing different backside boundary conditions.

This was tested by making ice samples of a set thickness, and performing a frequency sweep to a penetration depth greater than the thickness of the ice. A supported 3ω sensor as described in Section I.b was used, with a polystyrene dielectric layer of approximately $1\mu\text{m}$ thick, obtained by applying a polystyrene in toluene solution directly to the sensor (as described in [26]). Ice samples were prepared on these sensors using shims of known thickness. The shims also supported a copper or plastic piece, materials with high and low thermal conductivities with relative to ice, respectively. Once the shims and backside were in place, water was pipetted into the gap, with capillary action causing the water to stay between the sensor and the backside layer. The water was then frozen by setting the temperature of the bottom of the glass substrate to -10°C . Once the ice sample was in place, a 3ω measurement was performed. Figure 8a shows this setup and the results of these measurements, along with vertical lines representing the frequencies corresponding to the penetration depth being equal to the full thickness and half the thickness of the sample.

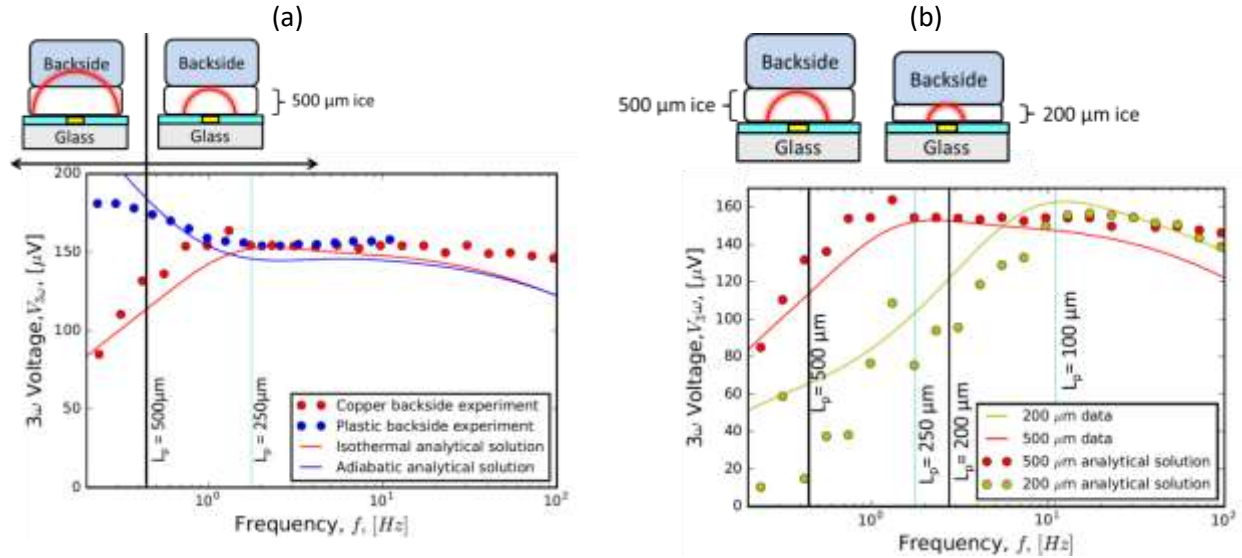


Figure 8: a) Frequency sweep of the out-of-phase 3ω voltage measured from an ice sample with two different backside boundary conditions. The penetration depth for 500 μm ice is denoted (black line), as well the frequency corresponding to 250 μm ice (cyan line). Analytical solutions (lines) for isothermal and adiabatic sample backsides using known sensor and sample properties are shown for comparison. b) Frequency sweep for ice samples of fixed thickness of (200 μm ,500 μm), both with copper plates on the back side which approximates an isothermal boundary condition. Frequencies corresponding to $L_p = 500, 250, 200,$ and $100\mu\text{m}$ are marked with vertical lines. Analytical solutions for an isothermal sample backside using sensor and sample properties are shown for comparison (lines).

The voltages in both Figure 8a and b match closely at penetration depths smaller than half the sample depth. At a frequency corresponding to approximately half the penetration depth, the 3ω voltage starts to change in ways that are consistent with the thermal conductivity of the backside layer playing a significant role. In the case of the plastic backside, the 3ω voltage increases as apparent thermal conductivity goes down; this is consistent with the measurement becoming increasingly sensitive to the low thermal conductivity backside. In the case of the copper backside, the measured 3ω voltage goes up, indicating the apparent thermal conductivity goes up as the thermal penetration depth goes through the sample and becomes more sensitive to the backside. Both trends qualitatively match expected results. Expected 3ω voltages are calculated using an analytical solution [16] and inputting known heater line and substrate properties, using isothermal and adiabatic sample backside boundary conditions. These results are shown with the experimental data above. This is done to show the limiting cases for backside boundary conditions and to provide context for the experimental results. The calculated voltages do not match experiments exactly, but qualitatively show the same trends as the experimental data. This matches well with expectations, since the thermal conductivity of the plastic is more than an order of magnitude higher than the ice, whereas the copper is two orders of magnitude higher. This indicates the experimental backsides should be close to adiabatic and isothermal backside boundary conditions for the sample. At higher frequencies (above ~ 20 Hz) the match between analytical solution and experimental data gets progressively worse as frequency increases. This may be due to error in measurements of the heater line width. When penetration depth becomes comparable to heater line width, the out-of-phase 3ω voltage is expected to deviate from the approximately constant voltage representing the penetration depth being well within the sample. In these plots, the 3ω analytical

solution begins to decrease at a frequency higher than the experimental data, indicating the real heater line may be wider than the model's input.

This experiment was also performed on ice samples with different thicknesses, with the same copper backside boundary condition in both cases. The results are shown in Figure 8b for 500 μm and 200 μm thick ice, with the 500 μm dataset being identical to what is presented in Figure 8a. In both cases, at penetration depths larger than ice thickness, the 3ω voltage deviates significantly from the 3ω voltage at penetration depths much less than the sample thickness. As expected, the 3ω voltage decreases at large penetration depths due to the high thermal conductivity copper backside. The 200 μm data has a large amount of noise at low frequencies, for reasons that are not entirely clear. Empirically, low frequencies are more prone to noise from many sources (whether from internal sources such as poor choice of lock-in amplifier settings, or external sources such as high building electrical demands), and this trial was not done more than once. The mismatch at between the analytical solution and experimental data is present the 200 μm data as well as the 500 μm data, further suggesting the heater line width was not measured correctly.

In both parts of Figure 8, the backside boundary condition is shown to become apparent at approximately L_p equal to half of sample thickness. This is qualitatively consistent with analytically predicted voltages, and it will be shown this general trend will play out in Chapter IV as well.

b. Lock-in response time

The lock-in amplifier is expected to respond to a step change in measured voltage with some delay. This is due to an RC time constant of the low pass filter, as discussed in Section I.c, which serves the purpose of filtering out noise signals in the measurement. This means that the measured third harmonic voltage response to a step change in thermal properties should also follow RC circuit behavior, if measured in real time. For a step change in thermal properties, the 3ω voltage will show 99% of the change within a set number of time constants, as determined by the roll off setting of the lock in amplifier (See

Table 1). In the case of the SRS lock-in amplifiers used in this experiment, 99% of the change will occur within 10 time constants when the maximum roll off setting is used.

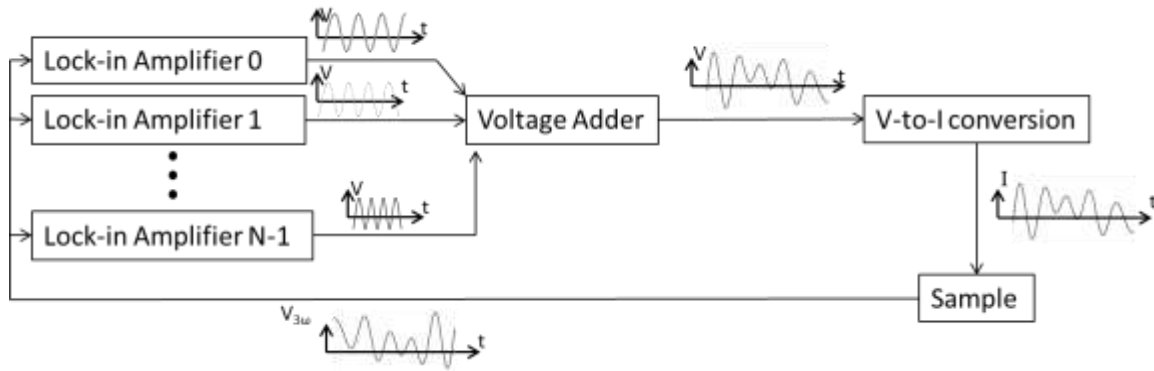


Figure 9: Schematic for the multi-frequency 3ω measurements, using multiple lock-in amplifiers

This was verified using the experimental configuration of Figure 9 using $N = 3$ lock in amplifiers (SRS830), with each lock-in amplifier's excitation signal set at 70 mV, or 7mA of current after V-to-I conversion. In these experiments a supported sensor (as shown in Figure 2c) was used, with the sample placed on the top half space of the sensor varying during the course of the experiment. The response time of the lock-in amplifiers was verified by measuring $V_{3\omega}$ continuously (~ 12 samples/second) for a bare sensor alone, and subsequently through the event of a room temperature water droplet being pipetted onto the 20°C sensor, approximating a step change in thermal properties as seen by the measurement. This experiment is shown in Figure 10a, with 0 on the time axis representing the time the water was pipetted onto the sensor. Due to the dielectric nature of the polystyrene layer, the water beaded upon placement, covering a radius of approximately 6mm, centered on the heater line. Since the maximum penetration depth in the experiment is 1.14mm (see Table 3), the water is expected to appear semi-infinite in all directions. The measurement is expected to detect a change in k_{apparent} from that of the sensor support on the bottom half space with air on the top half space, to the sensor support on the bottom half space and water on the top half space. This change represents an increase in the apparent thermal conductivity as measured by the sensor. The measured $V_{3\omega}$ is expected to decrease, as the measured voltage is inversely proportional to the apparent thermal conductivity (equation (5)), and the half space above the sensor is increasing in thermal conductivity from k_{air} to k_{water} .

Figure 10b shows the in-phase $V_{3\omega}$ response, with the time normalized by the lock-in time constant of each channel. $V_{3\omega}$ is normalized by setting the voltage at $t = 0$ to be 0, and the voltage at $t = 140$ to be 1. The RC time constants used for excitation frequencies of 0.103 Hz, 1.03 Hz and 10.3 Hz were 10 seconds, 1 second, and 0.3 seconds, respectively. These were selected to be as low as possible while preserving the stability of the measurement. The roll-off setting on the lock-in amplifiers was set to 24dB/oct. Though the curves do not overlay perfectly, all 3 exhibit behavior resembling that of an idealized RC circuit. The ideal RC circuit behavior is plotted, with the filter order of the lock-in amplifier taken into account.

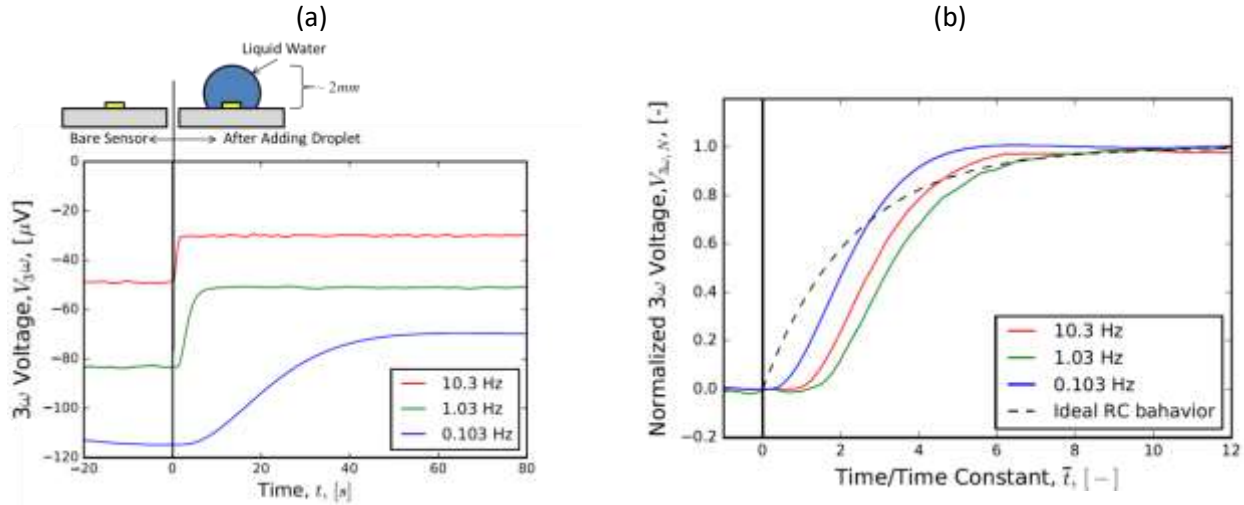


Figure 10: Panel a) Time response of in-phase 3ω voltage to placement of room temperature water droplet. This corresponds to an increase in apparent thermal conductivity, as monitored by 3 simultaneously measured frequencies. Panel b) shows the same data sets with time normalized by lock in time constant, and in-phase 3ω voltage normalized by starting ($t = 0$) and ending (average from $t = 140$) voltages. The 3 curves exhibit similar behavior to the idealized RC circuit.

Time constant takes on new importance in transient measurements, presenting a tradeoff between response time and measurement noise. A low time constant will yield faster response time but with greater noise. When monitoring events in real time, it is desirable to have the fastest response time possible while limiting measurement noise. This presents potential challenges for application of this technique.

c. Real time monitoring of freezing and thawing water

The ability of the 3ω technique to sense phase change in real time was verified by monitoring a water droplet as it underwent a phase change event, namely between liquid and solid. The same water droplet and time constants of Figure 10 were used for the freezing test. The third harmonic of electrical excitation frequencies of 10.3, 1.03 and 0.103 Hz were monitored simultaneously for these measurements. The associated penetration depths are shown in Table 3. The RC time constants used for excitation frequencies of 0.103 Hz, 1.03 Hz and 10.3 Hz were 10 seconds, 1 second, and 0.3 seconds, respectively.

Table 3: Penetration depths for measured electrical excitation frequencies, as defined in equation (4)

Frequency [Hz]	Penetration Depth in Water [mm]	Penetration Depth in Ice [mm]
0.103	1.14	1.44
1.03	0.361	0.457
10.3	0.114	0.144

Using the supported 3ω sensor of Figure 2c, the 3 $V_{3\omega}$ signals were monitored continuously as the temperature of the stage was set to 20°C , then suddenly lowered to -10°C , triggering freezing of the droplet. After the temperature and measured voltages stabilized, the temperature of the stage was then

suddenly increased back to 20°C, thawing the frozen droplet. The results of these measurements are shown in Figure 11a. The frozen or thawed state of the droplet was confirmed by camera images.

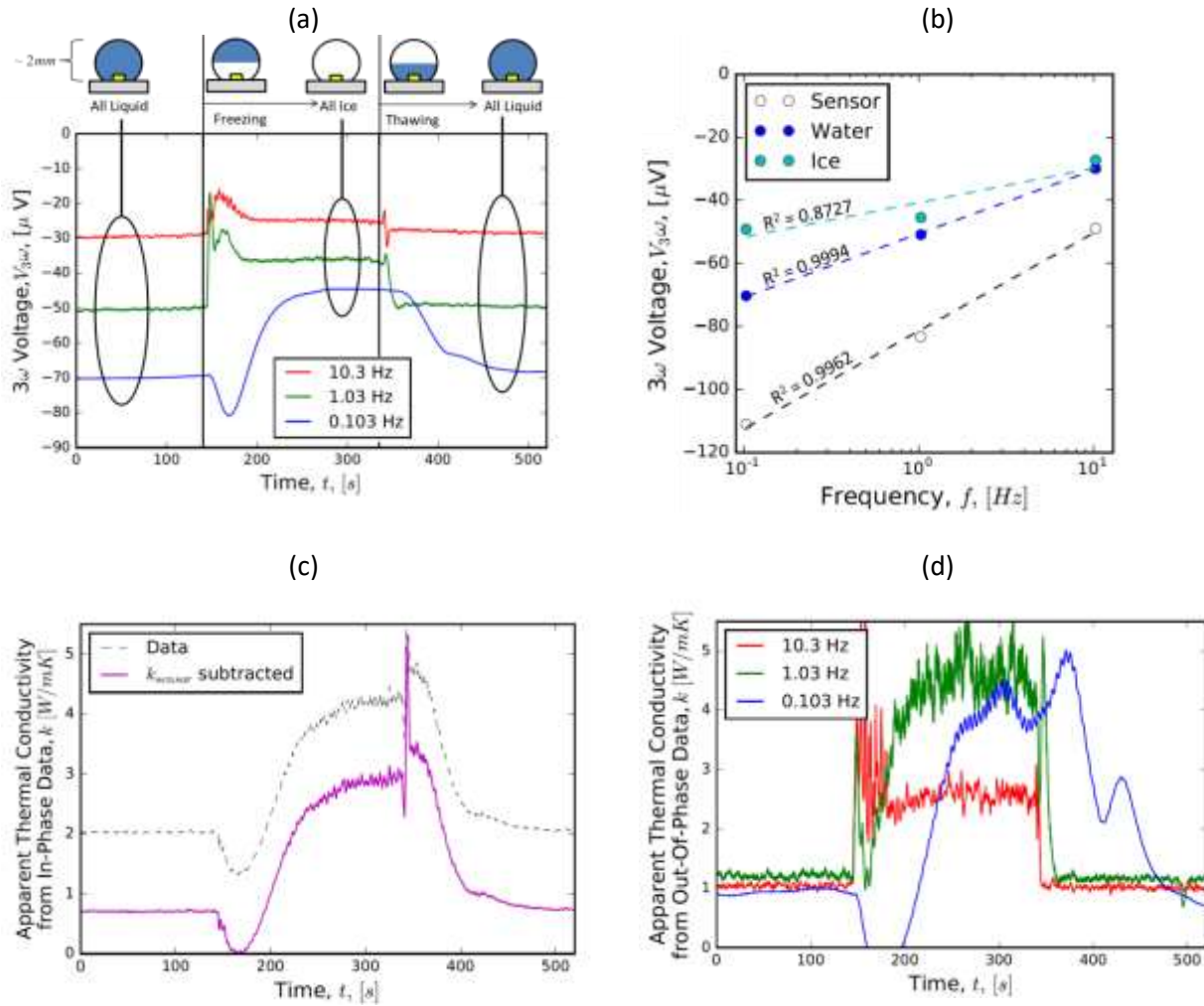


Figure 11: a) Real time monitoring of in-phase 3ω voltage during freezing and thawing test of water. b) Averaged in-phase voltages used for calculation of thermal conductivity (from panel a and Figure 10a). c) Corresponding thermal conductivity evolution over time, as calculated by the slope method (equation (6)) using in-phase 3ω voltage data collected during the experiment. d) Real time thermal conductivity as calculated from the out-of-phase 3ω voltage for each frequency (equation (6)). In panel d the thermal conductivity of the sensor (1.32 W/m-K), as measured from the in-phase data, has been subtracted.

Table 4: Summary of thermal conductivities extracted from water freezing and thawing data in Figure 11.

	k_{sensor} [W/m-K]	k_{liquid} [W/m-K]	k_{ice} [W/m-K]
Time Averaging Window	t = -55 - 0s (Figure 10)	t = 1 - 100s (Figure 11)	t = 280 - 330s (Figure 11)
In-Phase Data	1.32	0.71	2.44
Out-of-Phase Data: 0.103 Hz	1.54	0.69	3.61
Out-of-Phase Data: 1.03 Hz	1.58	0.92	4.33
Out-of-Phase Data: 10.3 Hz	1.36	0.99	2.51
Handbook	1.29 (Amorphous SiO ₂ , 20 °C) [20]	0.60 (Water, 20 °C) [21]	2.30 (Ice, -10 °C) [21]
Error: In-phase data versus handbook	2%	18%	6%

The in-phase voltages are stable in the regions corresponding to fully liquid water and fully solid ice. The measured voltages corresponding to the two regions of fully liquid water (t = 0-100s and the final voltages measured in the trial, at t = 520s) match for each of the frequencies to within 3%, suggesting the precision and repeatability of the measurements. The difference between each frequency's voltage in the fully liquid region and voltage in the fully solid region is greater than 15%, demonstrating the ability of the measurement technique to distinguish between frozen and thawed phases.

The transient regions of Figure 11a and d appear prone to overshoot. The reasons for this are not entirely clear, but latent heat of phase change is suspected. Qualitatively, if the overshoot regions are excluded, the data shows the expected trend of decreasing measured voltage when the water droplet freezes. This decreasing 3ω voltage corresponds to a decreasing heater line temperature, indicating an increase in effective thermal conductivity as seen by the sensor.

Figure 11b plots the average voltages corresponding to the 3 steady states the sensor was in: sensor in air (not shown in Figure 11a), sensor with liquid water, and sensor with ice. The voltages used are averaged from the leftmost "all liquid" region (t = 0 to 100 seconds), and "all ice" region (t = 280 to 330 seconds) in Figure 11a. The sensor (with air in the top half space) voltages come from Figure 10 (which is from the same experimental session), in the "bare sensor" region (-55 to 0 seconds). These 3ω voltages are used to calculate thermal conductivities of the water. As described in Section I.e, the thermal conductivity can be calculated from either the in-phase or out-of-phase data, with the in-phase data expected to be more robust. The calculated values are summarized in

Table 4. Figure 11c shows the thermal conductivity calculated from the slope method (equation (6)) as the experiment occurs. The black dotted line shows the raw thermal conductivity number, while the magenta line is the calculated thermal conductivity after subtracting the thermal conductivity of the sensor, as described in Section I.e. Figure 11d shows the out-of-phase voltages replotted as thermal conductivity, using equation (5).

From the trial's initial data with the bare sensor by itself (Figure 10), the calculated thermal conductivity is 1.32 W/m-K from the slope of the in phase data, and ranges from 1.36 to 1.58 W/m-K for the out-of-phase data (compared to handbook value of amorphous SiO₂ of 1.29 W/m-K [20]). Analyzing the slopes of liquid water data points, using the BMA and subtracting the measured sensor thermal conductivity, yields a thermal conductivity of water of 0.71 W/m-K from the in-phase data, and 0.69 – 0.98 W/m-K from the out-of-phase data. In comparison to the literature values at 20°C of 0.60 W/m-K this agrees, though not well. The calculated thermal conductivity of ice from the slope method is more consistent with handbook values (2.30 W/m-K), with a measured value of 2.43 W/m-K. The calculated thermal conductivity of the ice from the out-of-phase data matches quite poorly, however, with a range of 2.51 - 4.32 W/m-K. The slope method (in-phase data) yields thermal conductivities that are less than 20% from handbook values (18% and 5.7% error for water and ice, respectively), though the out-of-phase calculation does not appear to yield useful results.

The measured thermal conductivities in these experiments may deviate from handbook values for several reasons. The most apparent is that the 3 frequencies do not all appear to be in the range in which the penetration depth is well contained in the sample while being much greater than the heater line width. Indeed, the penetration depth for ice and water at 0.103 Hz is at least half of the approximate thickness, and at 10.3 Hz the penetration depth is only 2-3x the heater linewidth. Both of these are not in the frequency range where the slope method should ideally be utilized. This is further evidenced by the fact that the out-of-phase voltages (which are inversely proportional to the calculated thermal conductivity) are not all the same, as would be expected in the frequency range over which the slope method would be calculated.

d. Monitoring frozen and thawed mouse liver

To demonstrate the utility and viability of this technique in on biological samples, a piece of mouse liver was monitored continuously in the same fashion as the water droplet of the previous section, with an identical identical freezing/thawing procedure on the same sensor. The mouse liver was approximately 3mm thick, and was wetted thick, and was wetted before placement to ensure intimate thermal contact (identical procedure to that used by Lubner et used by Lubner et al. [26]). The raw data is shown in Figure 12a. Figure 12b shows the steady voltages used for calculating used for calculating the in-phase thermal conductivities presented in

Table 5. These voltages span -200 to -100s (not shown in the figure) for the sensor with air in the top half space, 50-100s for the liver data, and 350-400s for the frozen liver data. There is less than 1% deviation between the liver data from 50-100s and the final data point for all 3 frequencies measured. The real-time calculated thermal conductivities are also presented above in Figure 11, with the calculated value from the slope method in Figure 12c, and from the out-of-phase values in Figure 12d.

This data exhibits the same qualitative trends as the water data of Figure 11, with decreasing 3ω voltages when the sample freezes. The overshoot at the beginning of freezing and thawing events is again believed to be due to latent heat of phase change. Measured thermal conductivity was calculated from the both in phase and out of phase data, as above. These calculations yield values which match closely with literature, with the sensor being measured at 1.28 W/m-K by the in-phase data, and 1.35 – 1.54 W/m-K by the out-of-phase data, matching well with the handbook value of 1.29 [20]. The measured thermal conductivities in this experiment match closely with the measured thermal conductivity of the same sensor in the water trials above. Using the BMA and subtracting the measured thermal conductivity of the sensor, a thermal conductivity of 0.60 W/m-K is measured for in-phase data of the thawed liver, and 0.57 – 0.70 W/m-K with the out-of-phase data. These compare reasonably to Lubner et al's [18] measurements of thawed mouse liver of 0.51 at 10°C (17% error for slope method). Similarly, Lubner et al measured thermal conductivity of frozen mouse liver to be 1.50 W/m-K at -20°C, comparing well to this data, in which the thermal conductivity is measured to be 1.80 W/m-K with the in-phase data (20% error from), and 1.87 -2.44 W/m-K using the out-of-phase data. The deviations in measured thermal conductivity from literature values are attributed to the same causes as in the previous section, with thermal penetration depths expected to be similar to water.

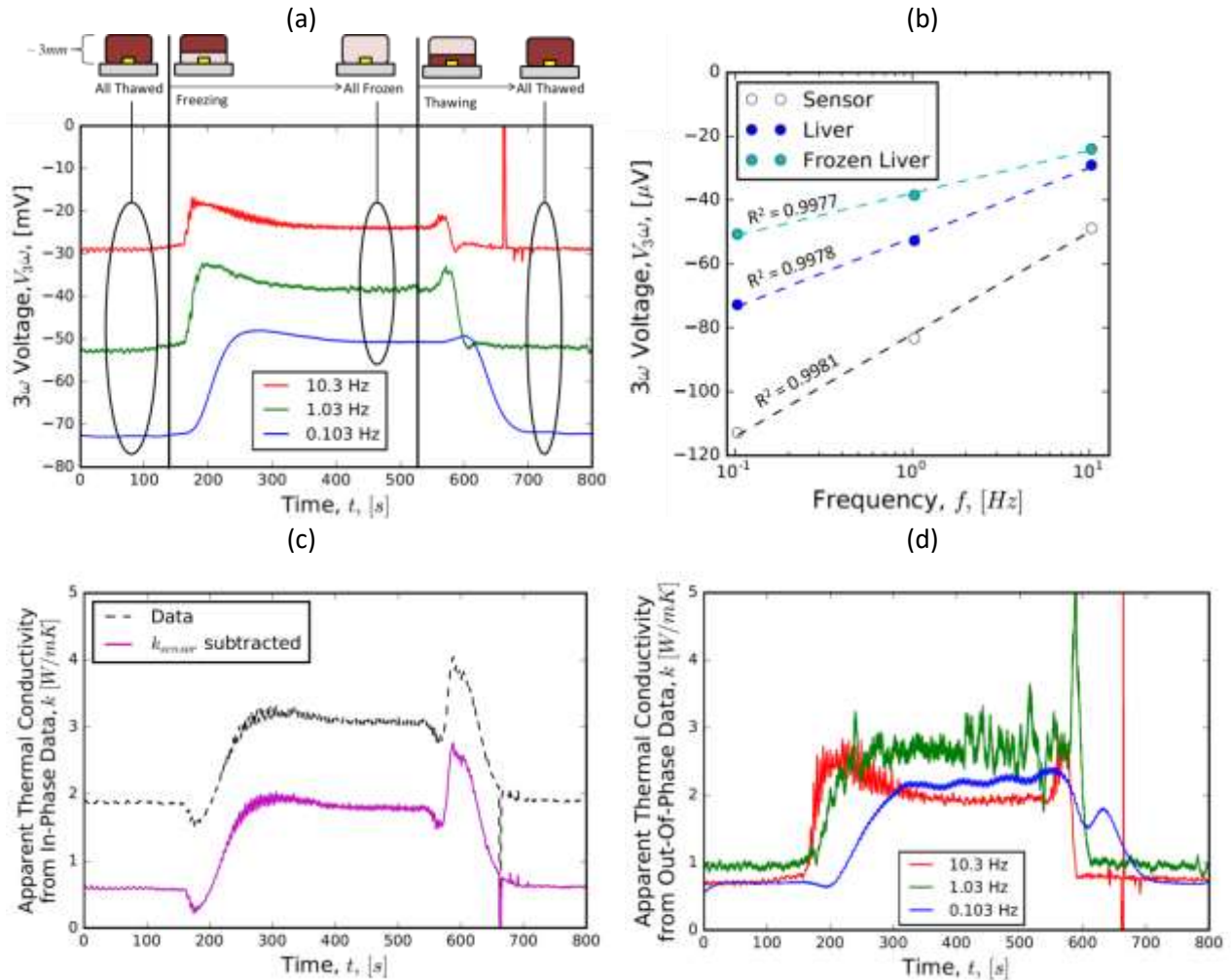


Figure 12: a) Real time monitoring of in-phase 3ω voltage during freezing and thawing test of mouse liver. b) Averaged in-phase voltages used for calculation of thermal conductivity (from panel a). c) The corresponding thermal conductivity evolution over time, as calculated by the slope method (equation (6)) using in-phase 3ω voltage data collected during the experiment from the . d) The real time thermal conductivity as calculated from the out-of-phase 3ω voltage for each frequency (equation (5)). In panel d the thermal conductivity of the sensor (1.28 W/m-K), as measured from the in-phase data, has been subtracted.

Table 5: Summary of thermal conductivities extracted from mouse liver freezing data from Figure 12.

	k_{sensor} [W/m-K]	k_{liver} [W/m-K]	$k_{\text{frozen liver}}$ [W/m-K]
Time Averaging Window	t = -55 - 0s (Figure 10)	t = 50 - 100s (Figure 12)	t = 350 - 400s (Figure 12)
In-Phase Data	1.28	0.60	1.80
Out-of-Phase Data: 0.103 Hz	1.43	0.57	2.08
Out-of-Phase Data: 1.03 Hz	1.54	0.70	2.44
Out-of-Phase Data: 10.3 Hz	1.35	0.66	1.87
Literature	1.29 (Amorphous SiO ₂ , 20 °C) [20]	0.51 (Unfrozen mouse liver [18])	1.50 (Frozen mouse liver [18])
	0.8%	17%	20%

e. Transient response to a distant event

The ability of the 3ω technique to detect an event occurring away from the sensor in real time was tested by pipetting a water droplet onto a layer of frozen agar gel in direct contact with the heater line. An 0.5% (by weight) agar gel sheet of approximately 0.4 mm thickness was placed on the sensor, and frozen at -20°C . Agar gel should have identical thermal conductivity to water at this concentration [22]. As indicated in the schematic of Figure 13a, at a later time, after the agar gel had reached equilibrium in a frozen state at -20°C , ($t = 0\text{s}$ in Figure 13a, c, and c) a droplet of deionized water was pipetted on top of the frozen agar gel sheet. This caused a change in apparent thermal conductivity (i.e., $k_{\text{agar}} \gg k_{\text{air}}$) in a region that only the lowest frequency is expected to be sensitive to, based on the penetration depths shown in Table 3. While the 1.03 Hz penetration depth is in the region that may be affected by the change in apparent thermal conductivity, it will be shown in subsequent sections that the in-phase data is expected to be less sensitive to changes in apparent thermal conductivity close to the penetration depth. It is notable that when the droplet was pipetted onto the frozen agar, all 3 frequencies exhibit voltage transients in Figure 13, as the system reaches thermal equilibrium. This is attributed to temperature transients in the system as the liquid water droplet freezes. The steady voltages were compared by taking the average voltages from times -115s to -15s (for the state before the remote event) and 135-235s (after the remote event) in Figure 13a. The 1.03 and 10.3 Hz datasets are essentially unchanged compared to their previous steady state values (less than 2% difference). On the other hand, the 0.103 Hz data changes in steady state value by 5% in the case of the in-phase voltage as seen in Figure 13a and b, and 45% in the case of the out-of-phase voltage (not shown) and corresponding thermal conductivity (Figure 13d).

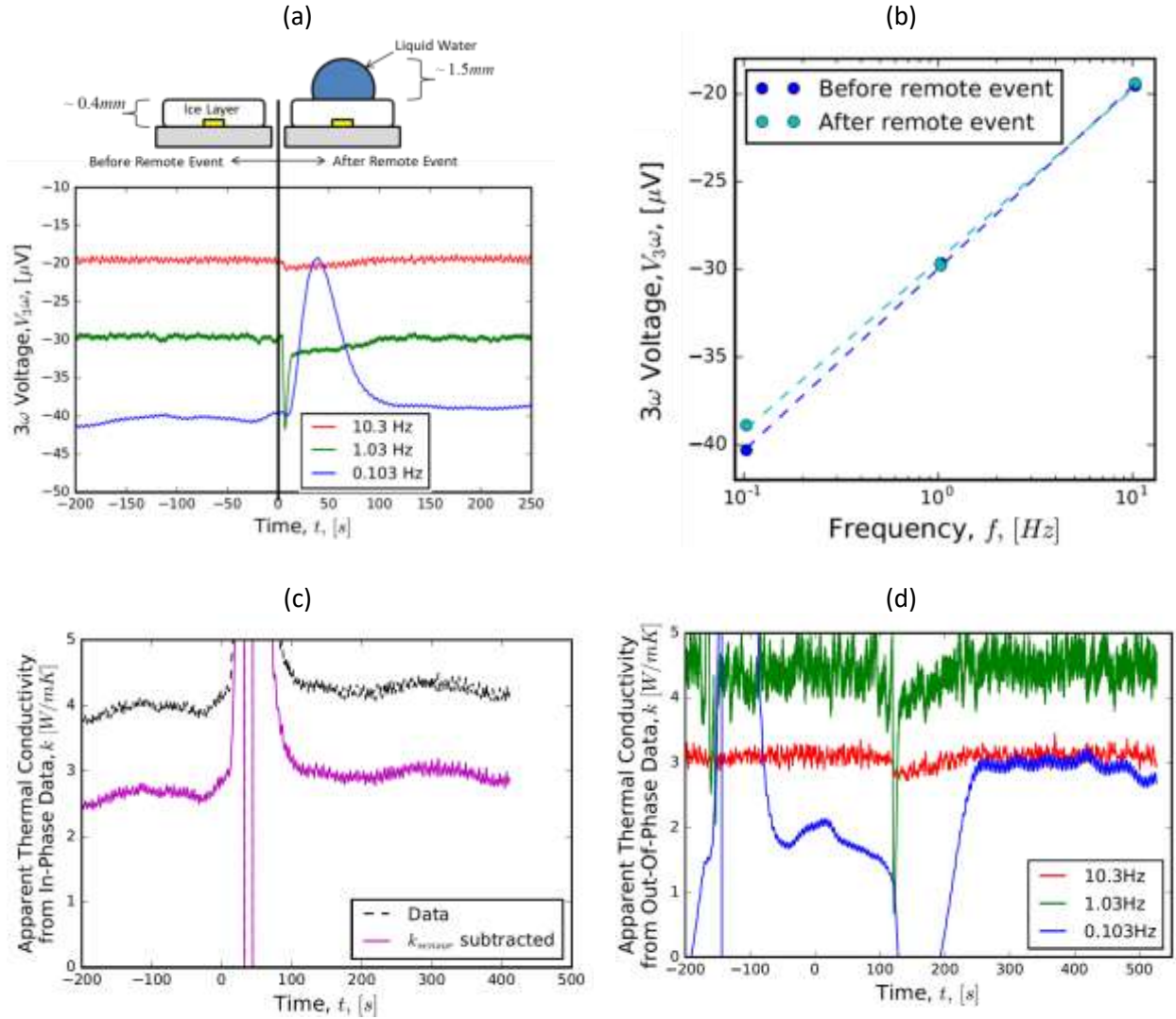


Figure 13: Thermal response to a remote event: placement of a water droplet on frozen agar gel (effectively equivalent to an ice layer, as indicated in the schematic) in contact with the heater line. a) Real time monitoring of in-phase 3ω voltage during the remote event. b) Averaged in-phase 3ω voltages used for calculation of thermal conductivity (from panel a). Corresponding thermal conductivity evolution over time, as calculated by the slope method using in-phase 3ω voltage data collected during the experiment. d) Real time thermal conductivity as calculated from the out-of-phase 3ω voltage for each frequency. In panel d the thermal conductivity of the sensor, as measured from the in-phase data in Figure 10 and Figure 11, has been subtracted.

Table 6: Summary of calculated thermal conductivities before and after a remote event

	$k_{\text{apparent, sample, before}}$ remote event [W/m \cdot K]	$k_{\text{apparent, sample, after}}$ remote event [W/m \cdot K]	Relative change in
In-Phase Data	2.66	2.92	9.8%
Out-of-Phase Data: 0.103 Hz	1.78	2.97	67%
Out-of-Phase Data: 1.03 Hz	4.40	4.48	2%
Out-of-Phase Data: 10.3 Hz	3.10	3.11	0.3%
Handbook (Ice, -10 °C) [21]	2.40	2.40	-

As in the preceding sections, the measured thermal conductivity can be calculated based on the slope method and out-of-method and out-of-phase voltages. These are summarized in

Table 6. The same supported 3ω sensor as the previous two experiments was used in this test. Thermal conductivity of the sensor was not directly measured in this experiment, but an average of the values calculated from in phase data from the previous 2 sections (1.30 W/m-K) was used. Because the sample does not extend through the penetration depth of the lowest frequency before the remote event, it is less meaningful to calculate a thermal conductivity based on the slope of the 3 frequencies or the out-of-phase data in this time region. However, comparing the calculated thermal conductivity before and after should verify if method qualitatively has behaved as expected. If the slope method calculation is done, the thermal conductivity shows an increase from 2.66 to 2.92 W/m-K, an increase of 9.8%. This shows the expected result, that the thermal conductivity increases when a portion inside the penetration depth of the top half space changes from air to ice.

Parts c and d of Figure 13 show the calculated thermal conductivity from in-phase and out-of-phase voltages, respectively. The out of phase measurement at 0.103 Hz is particularly noisy, for reasons that are not fully understood. This may be due to errors in setting lock-in time constants during the experiments. As with the in-phase numbers, average voltages from times -115s to -15s are used for the state before the remote event and 135 to 235s for the state after the remote event. Similar to in Section III.b, the out-of-phase thermal conductivities match handbook values poorly, though the lowest frequency the value matches the closest, and increases after the remote event as expected. This may be coincidence, however, as the measured voltage is very noisy.

IV. Front tracking

In this chapter, an experimental study on tracking a moving interface in real time using 3ω voltages is detailed. While the previous chapter's experiments illustrate the capability of the 3ω technique to sense step changes in thermal properties, this chapter aims to show the ability of the technique to measure thermal properties changing gradually. Tracking continuously changing thermal properties requires more nuanced analysis, as well as greater experimental precision, both in the physical setup and in the electronic settings. To create an idealized system where an interface moves slowly and constantly, a customized setup was designed and built. This setup will be detailed in the next section.

As Figure 14 illustrates, the goal of this study was to determine the distance d between a sensing heater and a remote interface. When L_p is larger than the depth of sample in one direction (d), the thermal response at the heater depends on the thermal diffusivity, α , of both material 1 and 2. This case is illustrated by L_{p1} in Figure 14a. If d exceeds the thermal penetration depth, the heater's thermal response is determined only by α of material 1, and material 2 cannot be sensed. This second case is illustrated by L_{p1} in Figure 14b, as well as L_{p2} in both figures. Comparing the L_{p1} scenarios in both panels, the difference in detected α will cause a change in temperature rise at the heater line, leading to a change in the 3ω voltage. In Figure 14, $\alpha_1 > \alpha_2$, leading to the distortion of the thermal penetration depth in material 2 in panel a. Thus, if the thermal properties are well known, d can be determined from the 3ω voltage. This is the essential principle underlying the experimental approach presented in the following sections. In experiments described below, the system was probed at multiple frequencies simultaneously, leading to greater sensitivity and larger ranges of d that can be detected. Furthermore, by performing these measurements continuously, the location of an interface is expected to be trackable as it moves.

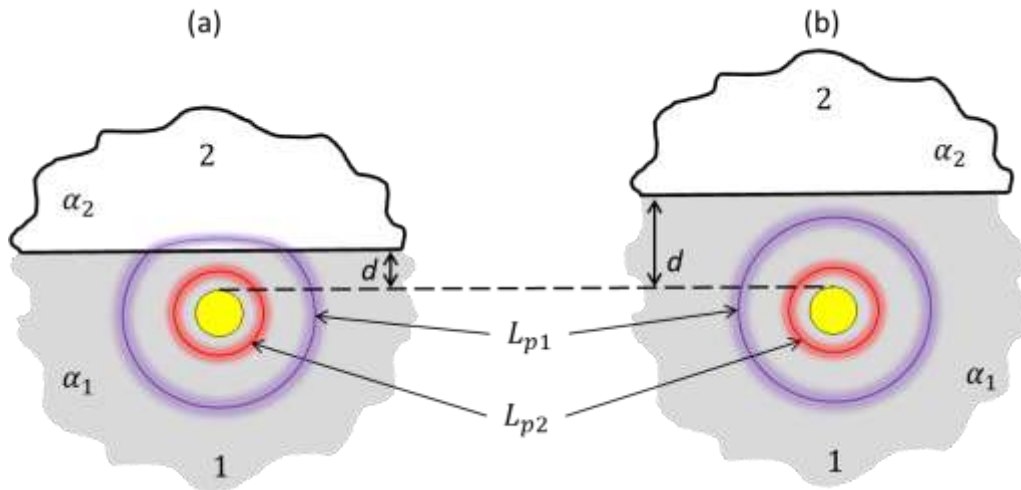


Figure 14: Principle of the front tracking measurement. Thermal penetration depths (purple, red) surrounding a heating wire (gold circle, long in the direction out of the page) embedded in two semi-infinite media (1, 2), with $\alpha_1 > \alpha_2$. In both panels, the L_{p2} is sensitive only to α_1 . In a), L_{p1} senses an effective thermal diffusivity that combines both α_1 and α_2 , whereas in b) L_{p1} is sensitive only to α_1 .

To create a wire sensor parallel to the oil-air front, a Wollaston wire (Sigmund Cohn Corporation) was etched to expose the platinum core of 5 μ m radius, leaving the wire with l_{sensor} of 30 mm. The maximum penetration depth used in the experiments is around 0.28 mm (Table 7). Thus, the effects of finite sensor length are negligible because the largest penetration depth is less than 1/6 of the sensor length [13]. Similarly, to avoid artifacts due to finite sample (oil) depth in any direction other than the positive y direction, $l_{cladding}$ was 10 mm and the sensor was placed approximately in the center of a well of w_{well} of 65 mm; additionally, the sensor was placed at h_{wire} of 20 mm. Because all relevant dimensions are large compared to maximum penetration depth used in the experiment, the oil can be treated as effectively infinite in the +x, +z, and -y direction as measured from the wire. This means the thermal information relevant to the measurement will not be affected by the presence of the posts or edges of the oil well.

Table 7: Thermal penetration depths for input current frequencies ($\omega/2\pi$) used in position tracking experiments

Frequency [Hz]	Penetration Depth in Oil [mm]
0.147	0.275
0.695	0.127
3.28	0.0582
15.5	0.0268

The ends of the silver cladding of the Wollaston wire were attached via electrically conductive silver epoxy (CircuitWorks CW2400) between two posts, one fixed (a stainless steel machine screw) and one flexible (22 AWG copper wire). The anchor point of the flexible post (at the top left of Fig. 2a) was slowly moved in the -z direction until the wire was completely in tension, verified by aligning the wire with a straight line in the eyepiece reticle of an AmScope WF10x/20 microscope. The continual state of tension in the wire was confirmed by camera images (AmScope MU500) during the experiments, in which the image of the wire created by reflection at the oil-air interface is parallel to the wire itself. As indicated in Figure 15b, the camera was placed at a small angle to the x axis in order to observe the reflection of the wire on the surface of the oil. This reflection was further used to align the wire axis to be parallel to the oil-air interface to within 1° of tilt (tilt measured with respect to the z axis of Figure 15). The position of the oil-air interface was manipulated by a syringe pump (WPI SP200I model, switching the lead wire configuration to make the pump run backwards during extraction trials).

In order to track the moving interface, the sensor was excited by a superposition of currents at four different frequencies. The thermal signals produced by simultaneous electrical excitation frequencies created a linear response in the thermal domain, and therefore the thermal response to each excitation was independent. This was ensured by multiplicatively spacing excitation frequencies by a factor of m (see Section II.c), chosen to be 4.78. The instrumentation to accomplish this is depicted in Figure 15c. Four separate lock-in channels were used, 3 from a Zurich Instruments HF2LI-MF and 1 from a Stanford Research Systems SR830. These instruments were connected to a PC and controlled by Python code. The reference voltage sine wave outputs from the four lock-in channels were superposed using the voltage adding capability of the Zurich HF2LI-MF, and then fed into a voltage-to-current conversion

circuit. The resulting current then flowed through the sample, composed of the sensing wire immersed in oil. The voltage drop across the sensing wire was measured using voltage leads connected at the posts as indicated in Figure 15a. With these connections, the measured voltage drop was dominated by the resistance of the exposed platinum wire ($R_{\text{sensor}} \approx 40 \Omega$). In order to increase sensitivity to the 3ω voltage, 1ω background subtraction was used on the superposed signal [1], but is not shown in Figure 15c. In all experiments the maximum roll off settings for the lock-in amplifiers were used (48 dB/octave for the Zurich HF2 and 24 dB/octave for the SRS830). The lock-in time constants (τ) were set to $9.42/\omega_{\text{excitation}}$, chosen as a compromise between minimal response time and experimental noise.

b. Calculating front position from raw 3ω data

In order to obtain a generalized relationship between the measured 3ω voltage, $V_{3\omega}$, and the position of the interface as represented by depth, d , the depth and voltage are nondimensionalized as follows:

$$\bar{D} \equiv d/L_p \quad (21)$$

$$\bar{V}_{3\omega} \equiv V_{3\omega}/V_{3\omega,\text{infinite}}, \quad (22)$$

where $V_{3\omega,\text{infinite}}$ is the 3ω voltage corresponding to a heater line surrounded by infinite oil on all sides ($d = \infty$), and d is the depth of oil as measured from the heater line in a sample that has semi-infinite oil on the opposite side. The two cases being compared are illustrated in Figure 16.

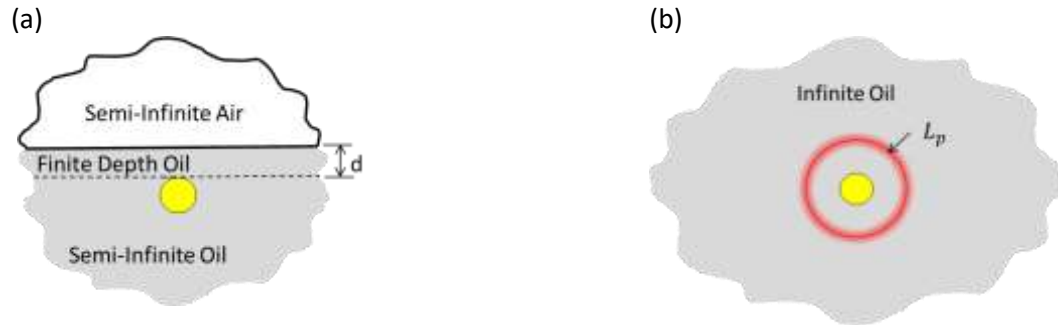


Figure 16: Schematic of the cases compared in dimensionless groups defined in equations (21) and (22).

In all models presented here convection effects are neglected. This is justified in mineral oil by calculation of the Grashof number [23]. Due to the temperature rise at the wire being less than 1 K, and the wire being of such small diameter, viscous effects are always expected to dominate buoyancy forces in the experimental conditions described here. The Grashof number was calculated to be $\sim 10^{-4}$ for even the most conservative case, indicating buoyancy forces that would create natural convection are negligible compared to the viscous forces in the oil. It was also verified that the bulk movement of the fluid has no effect on the measured voltage in each trial by confirming that the measured 3ω voltage remained unchanged when the pump was turned off. This was tested by stopping the pump and waiting for 20+ lock-in time constants. In each case there was no detectable change to measured voltage. Similarly, natural convection in air is neglected. The Gr in air was calculated to be $\approx 1e-2$ in the most conservative case, again indicating that natural convection can be neglected as a path of heat transfer in the problem.

In the efforts for modeling the relationship between the dimensionless groups defined by equations (21) and (22), idealized cases were used to investigate the behavior of the system before attempting to model the real experimental configuration. The starting place was the known analytical solution for 3ω voltage of a line heater in layered substrate [16], using the BMA detailed in Section I.e, with an adiabatic backside boundary condition on the top layer modeling semi-infinite mineral oil on the bottom side of the heater line and varying the top layer thickness from \bar{D} of 0 to 5 produced the plots shown in Figure 17.

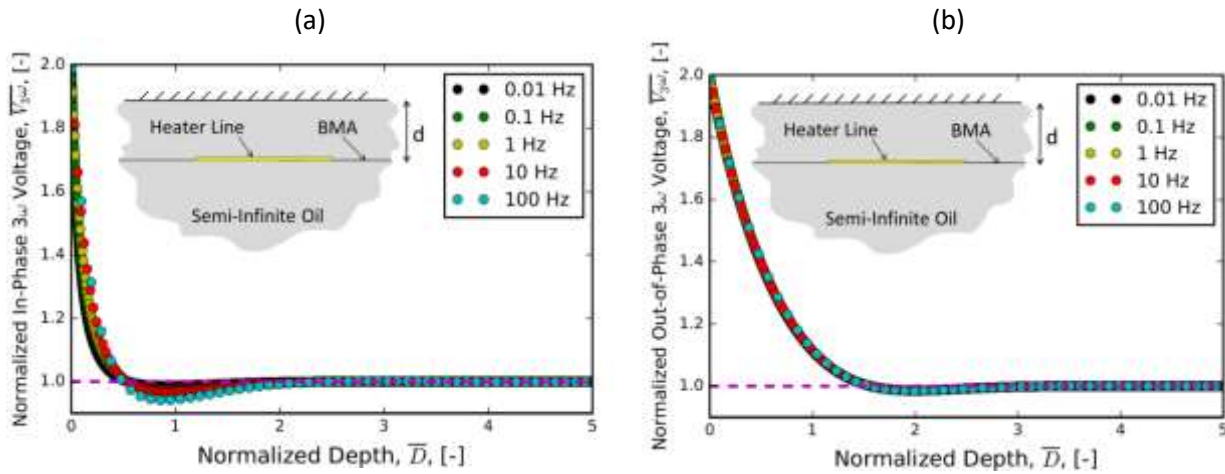


Figure 17: Comparison between in-phase (a) and out-of-phase (b) relationships between normalized depth and normalized 3ω voltage as defined in equations (21) and (22). Simulations are for a strip heater with $5\mu\text{m}$ half width. A line at $\bar{V}_{3\omega} = 1$ is shown for aid in interpretation.

With the simulation configuration of an adiabatic top backside, the results match the expected result of $\bar{V}_{3\omega}$ going from 2 (in the single sided oil case), to 1 in the double sided oil case, representing a doubling in the apparent thermal conductivity as measured by the strip heater. The above figure shows the out-of-phase voltage has a larger range of depths it will be sensitive to. This is illustrated by the range of normalized depth \bar{D} for which the normalized 3ω voltage $\bar{V}_{3\omega}$ is greater than 1. In data processing, if repeated values of $\bar{V}_{3\omega}$ are neglected, the range of \bar{D} for which a position can be calculated is $\bar{D} = 0 - 0.5$ in the case of in-phase data, and $\bar{D} = 0 - 1.5$ for out-of-phase data. Above these ranges, values of $\bar{V}_{3\omega}$ are not unique to one value of \bar{D} . In the experiments that follow, out-of-phase 3ω data is used for position tracking because of the greater range of depths that can be sensed.

It was found though COMSOL simulation that, when L_p is much larger than the heater line width, and much smaller than the sample thickness, a strip heater with half width $11.2\mu\text{m}$ gives the same temperature rise as a cylindrical heater of $5\mu\text{m}$ radius, if both are immersed in a semi-infinite medium. This result is verified analytically in Section IV.d below. The results of Figure 17a, oil with adiabatic backside, are shown again in Figure 18: Relationship between normalized depth and normalized voltage as defined in equations (21) and (22). Simulation configurations for a strip heater with $11.2\mu\text{m}$ half width (a,b)) and $5\mu\text{m}$ radius cylindrical heater c) are shown on their respective plots and are all infinitely long in the direction out of the page. a) Analytically calculated relationship for a line heater in an oil bath with an adiabatic boundary condition to approximate the surrounding air. b) Line heater analytical result with the finite thermal conductivity of air taken into account. Both a) and b) assume no

convection occurs, and use the BMA. c) Results of a 2D FEM simulation of cylindrical heater immersed in oil, as well as simulation results from the 1 Hz line heater analytical solution (from b)). d) Error between the FEM simulations for the cylindrical heater and the line heater analytical solution, i.e. the difference between points and line in c).

a. Figure 18: Relationship between normalized depth and normalized voltage as defined in equations (21) and (22). Simulation configurations for a strip heater with $11.2\mu\text{m}$ half width (a,b)) and $5\mu\text{m}$ radius cylindrical heater c) are shown on their respective plots and are all infinitely long in the direction out of the page. a) Analytically calculated relationship for a line heater in an oil bath with an adiabatic boundary condition to approximate the surrounding air. b) Line heater analytical result with the finite thermal conductivity of air taken into account. Both a) and b) assume no convection occurs, and use the BMA. c) Results of a 2D FEM simulation of cylindrical heater immersed in oil, as well as simulation results from the 1 Hz line heater analytical solution (from b)). d) Error between the FEM simulations for the cylindrical heater and the line heater analytical solution, i.e. the difference between points and line in c).

b replaces the adiabatic backside (of Figure 18: Relationship between normalized depth and normalized voltage as defined in equations (21) and (22). Simulation configurations for a strip heater with $11.2\mu\text{m}$ half width (a,b)) and $5\mu\text{m}$ radius cylindrical heater c) are shown on their respective plots and are all infinitely long in the direction out of the page. a) Analytically calculated relationship for a line heater in an oil bath with an adiabatic boundary condition to approximate the surrounding air. b) Line heater analytical result with the finite thermal conductivity of air taken into account. Both a) and b) assume no convection occurs, and use the BMA. c) Results of a 2D FEM simulation of cylindrical heater immersed in oil, as well as simulation results from the 1 Hz line heater analytical solution (from b)). d) Error between the FEM simulations for the cylindrical heater and the line heater analytical solution, i.e. the difference between points and line in c).

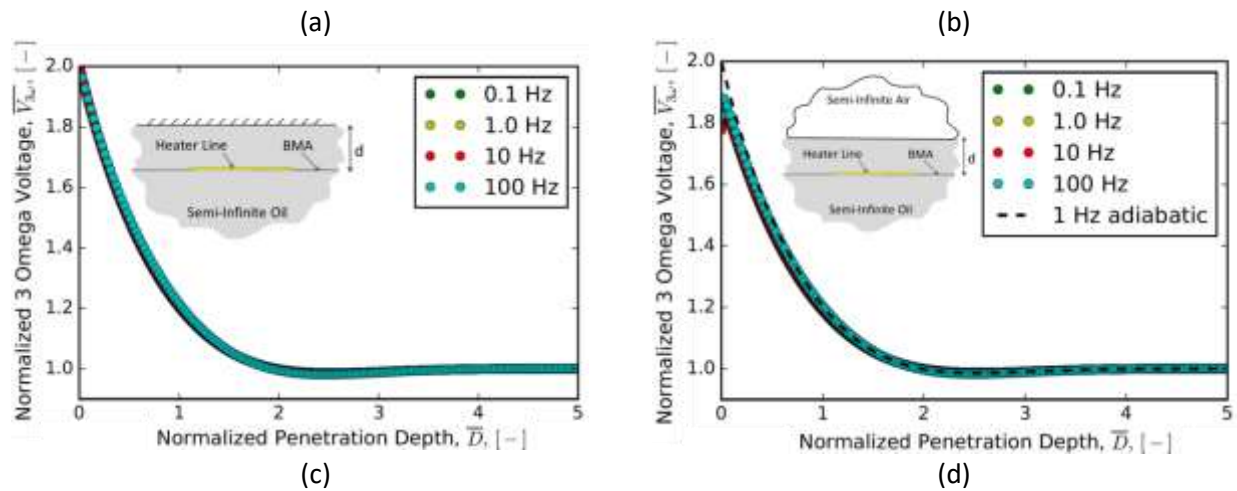
a) with semi-infinite air (quiescent, no convection). As expected, at small \bar{D} the $\overline{V_{3\omega}}$ does not go all the way to 2, due to the finite (though small) thermal conductivity of air. As the penetration depth extends further into the air backside, the apparent thermal conductivity should decrease. This is illustrated by the solution for the air backside deviating from the adiabatic backside solution when $\bar{D} < 1$ ($d < L_p$), and only deviating significantly when $\bar{D} \ll 1$. For the cylindrical heater with finite d an analytical solution could not be obtained. Instead, 2D FEM was performed in COMSOL to obtain a relationship between $\overline{V_{3\omega}}$ and \bar{D} . Figure 18: Relationship between normalized depth and normalized voltage as defined in equations (21) and (22). Simulation configurations for a strip heater with $11.2\mu\text{m}$ half width (a,b)) and $5\mu\text{m}$ radius cylindrical heater c) are shown on their respective plots and are all infinitely long in the direction out of the page. a) Analytically calculated relationship for a line heater in an oil bath with an adiabatic boundary condition to approximate the surrounding air. b) Line heater analytical result with the finite thermal conductivity of air taken into account. Both a) and b) assume no convection occurs, and use the BMA. c) Results of a 2D FEM simulation of cylindrical heater immersed in oil, as well as simulation results from the 1 Hz line heater analytical solution (from b)). d) Error between the FEM simulations for the cylindrical heater and the line heater analytical solution, i.e. the difference between points and line in c).

c indicates that the frequency independence of the relationship between $\overline{V_{3\omega}}$ and \overline{D} does not hold exactly in the case of a cylindrical heater, with different frequencies having slightly different functional relationships. This figure suggests that the previous solutions could be used for the cylindrical heater in oil, but with a $\sim 10\%$ error (see Figure 18: Relationship between normalized depth and normalized voltage as defined in equations (21) and (22). Simulation configurations for a strip heater with $11.2\mu\text{m}$ half width (a,b)) and $5\mu\text{m}$ radius cylindrical heater c) are shown on their respective plots and are all infinitely long in the direction out of the page. a) Analytically calculated relationship for a line heater in an oil bath with an adiabatic boundary condition to approximate the surrounding air. b) Line heater analytical result with the finite thermal conductivity of air taken into account. Both a) and b) assume no convection occurs, and use the BMA. c) Results of a 2D FEM simulation of cylindrical heater immersed in oil, as well as simulation results from the 1 Hz line heater analytical solution (from b)). d) Error between the FEM simulations for the cylindrical heater and the line heater analytical solution, i.e. the difference between points and line in c).

d) induced into the position data. To obtain a convenient mathematical form with much less than 10% error, the numerical results from tested frequencies were fit with an empirical 5 parameter fit of the form

$$\overline{V_{3\omega}} = a e^{-g\overline{D}} \cos(p\overline{D} - q) + s, \quad (23)$$

where the parameters a , g , p , q and s are all functions of ω . Each frequency was fit with separate parameters. This empirical $\overline{D}(\overline{V_{3\omega}}, \omega)$ interpolating function has errors of less than 1% as compared to the FEM calculations presented in Figure 18c, and is used to calculate position in the experiments presented below.



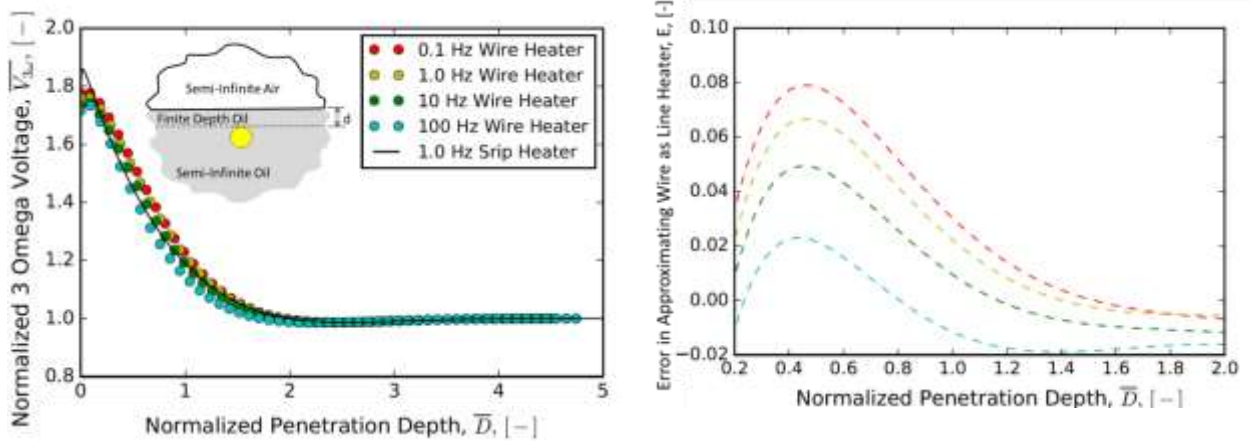


Figure 18: Relationship between normalized depth and normalized voltage as defined in equations (21) and (22). Simulation configurations for a strip heater with $11.2\mu\text{m}$ half width (a,b)) and $5\mu\text{m}$ radius cylindrical heater c) are shown on their respective plots and are all infinitely long in the direction out of the page. a) Analytically calculated relationship for a line heater in an oil bath with an adiabatic boundary condition to approximate the surrounding air. b) Line heater analytical result with the finite thermal conductivity of air taken into account. Both a) and b) assume no convection occurs, and use the BMA. c) Results of a 2D FEM simulation of cylindrical heater immersed in oil, as well as simulation results from the 1 Hz line heater analytical solution (from b)). d) Error between the FEM simulations for the cylindrical heater and the line heater analytical solution, i.e. the difference between points and line in c).

c. Heater half width producing the same temperature rise as wire heater of fixed radius

Here, it is desirable to obtain the relationship between heater line half width and wire radius that will produce the same temperature rise at the surface of a heater, when L_p is much larger than the heater line width, and much smaller than the sample thickness (the region in which the 3ω technique is commonly used). To do this, the thermal transfer functions [20] for the two cases can be compared. Thermal transfer functions (Z) are defined as

$$\theta = ZQ \quad (24)$$

In these equations, θ and Q represent temperature rise and heat flow, respectively. In the case of a wire heater in an infinite medium, the general solution form of the cylindrical heat equation is

$$\theta(r, t) = cK_0(\beta r), \quad (25)$$

where K_0 is a 0th order modified Bessel function of the second kind [4] [15]. In this equation,

$$\beta = \sqrt{\frac{i2\omega}{\alpha}}. \quad (26)$$

The heating of the sensor is described as

$$Q = -kA \left[\frac{\partial T}{\partial r} \right]_{r=r_0} = -k 2\pi R L \beta r c \frac{K_1(\beta r_0)}{K_0(\beta r_0)}. \quad (27)$$

Here r_0 here represents the radius of the heating wire, and r represents the radial coordinate. After a first order logarithmic expansion of the Bessel functions, as in [4], this can be rewritten as

$$Z_{wire} = \frac{-\frac{1}{2}}{2\pi kL} \left[\ln 2\omega + \ln \left(\frac{r_0^2}{\alpha} \right) + \frac{i\pi}{2} + 2\gamma - \ln(4) \right]. \quad (28)$$

This is compared to the transfer function for the line heater [32]

$$Z_{wire} = \frac{-\frac{1}{2}}{2\pi kL} \left[\ln 2\omega + \ln \left(\frac{b^2}{\alpha} \right) + \frac{i\pi}{2} + 2\gamma - 3 \right], \quad (29)$$

where b is heater half width. Comparing the two expressions yields

$$b = \frac{e^3}{4} r_0 = 2.240 r_0. \quad (30)$$

This confirms the numerical result above that a heater line of half width $b = 2.240 r_0$ and a heating wire with radius r_0 will produce the same temperature rise.

d. Data processing and results

Using the experimental setup presented in Figure 15, 3ω voltage data was collected as the oil-air interface moved away (d increasing; oil infusion) and towards (d decreasing; oil extraction) the wire sensor. The time constants (τ) were set to $9.42/\omega_{excitation}$, chosen to minimize response time. The additional noise expected as a result of small τ was offset with additional processing after the experiment was complete. Post-processing was done by applying 3 consecutive moving averages to each $V_{3\omega}(t)$ time series to filter out residual periodic noise. The time window for each moving average was chosen based on a fast Fourier transform (FFT) of the raw data, with the moving average being applied to a window of $2\pi/\omega_{noise}$, where ω_{noise} was determined by highest FFT peak, outside of the targeted signal at $\omega \rightarrow 0$. The voltage readings corresponding to times of $t + \frac{2\pi}{\omega_{noise}}$ to $t - \frac{2\pi}{\omega_{noise}}$ were averaged to find a moving averaged voltage at time t .

The smoothed $\overline{V_{3\omega}}$ data was then converted to a position by inverting the $\overline{V_{3\omega}} = f(\overline{D}, \omega)$ relationship, using the interpolating functions of the form of equation (23). The $V_{3\omega, semi-infinite}$ value, taken from each trial's fully infused state at each frequency, is assumed to approximate $V_{3\omega, infinite}$, because of the large value of $d \gg L_p$ at the fully infused state. The range of $\overline{V_{3\omega}}$ between 1.15 and 1.6 is used to calculate depth. Referring to Figure 18: Relationship between normalized depth and normalized voltage as defined in equations (21) and (22). Simulation configurations for a strip heater with $11.2\mu\text{m}$ half width (a), b)) and $5\mu\text{m}$ radius cylindrical heater c) are shown on their respective plots and are all infinitely long in the direction out of the page. a) Analytically calculated relationship for a line heater in an oil bath with an adiabatic boundary condition to approximate the surrounding air. b) Line heater analytical result with the finite thermal conductivity of air taken into account. Both a) and b) assume no convection occurs, and use the BMA. c) Results of a 2D FEM simulation of cylindrical heater immersed in

oil, as well as simulation results from the 1 Hz line heater analytical solution (from b)). d) Error between the FEM simulations for the cylindrical heater and the line heater analytical solution, i.e. the difference between points and line in c).

c, this range was selected for two reasons: it avoids the non-monotonic nature of the $\bar{D} = f(\bar{V}_{3\omega})$ function in regions around $\bar{V}_{3\omega} = 1.8$ and $\bar{V}_{3\omega} = 1$, and empirically, this region has the least noisy data after post-processing.

A representative time series for one frequency is shown in Figure 19a after applying the moving average but before converting the voltage at each time into a position. The start time for the pump is marked with a blue vertical line, and the upper and lower bounds accepted into the position calculation are shown with horizontal black lines ($\bar{V}_{3\omega}$ of 1.15 and 1.6). This data set is from the infusion trial, for the monitored frequency of 0.147 Hz.

Due to the small penetration depths used in the experiments (penetration depth at the highest frequency is 26.8 μm), the front velocity induced by the syringe pump was kept very slow, ≈ 95 and ≈ 380 nm/s. This was done to create a quasi-static measurement environment in order to ensure that the movement through a penetration depth's sensitivity region occurs over several lock-in time constants.

The position of the oil-air front, $d(t)$, was verified by images from the camera, and both are plotted in Figure 19b-e. The position as measured by the camera is shown with individual image points as dots, and the fit to 8 images taken over a long time period as a dotted line. The camera images were converted to position by converting number of pixels between the wire and its reflection to a length, using the silver cladded wire of known diameter as a pixel to distance calibration. This image processing method did not work when the oil surface was in contact with the wire cladding due to meniscus distortions. For this reason, for infusion tests the camera images for $d < 40\mu\text{m}$ depth are not included in the presented camera data. During infusion tests, it was observed that the pump took some time to begin pumping at the specified infusion rate, attributed to a stiction effect.

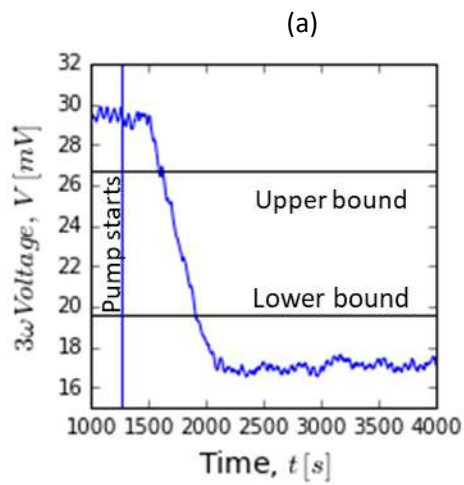
Figure 19b shows the front position calculated from the processed 3ω data, compared to the position measured by the camera images, for an extraction velocity setting of 383 nm/s (i.e., $d(d)/dt = -383$ nm/s). Due to the chosen frequency spacing, there is some overlap between calculated positions for each frequency. From the acceptable range of $\bar{V}_{3\omega}$, the position is calculated from 10 μm (minimum at the highest frequency), to 360 μm (the maximum of the lowest frequency). Figure 19c and d show similar results, for oil infusion with front velocity of 376 nm/s and oil extraction with front velocity of 95.1 nm/s. In Figure 19b-d, $t = 0$ corresponds to when the pump is turned on.

Figure 19e shows comparison of the 3 data sets. In this plot, line style represents the trial, and line color represents frequency (as in Figure 19b-d). The plot shows the close agreement between the position calculated from the camera images and the position calculated by the 3ω data, as well as the precision between the 3 data sets. From the data in Figure 19b-d, it can be computed that from the calculated position curves there is an RMS error in calculated position between the 3 trials of 17.6 μm . The error is calculated via the root mean squared of the absolute difference between the fit of position as measured by the camera and position as calculated by the 3ω data, equally weighted at every time step. Between

the 3 trials, there is a maximum deviation between position as measured by the camera and predicted position by 3ω data of $46.7\mu\text{m}$. Table 8 summarizes these results, and shows the RMS error ranges from 11.6 to $29.3\mu\text{m}$ across the three trials.

Table 8: Summary of 3 position tracking trials

Front Velocity	RMS error in position	Maximum error in position
-383 nm/s	11.6 μm	25.2 μm
376 nm/s	29.3 μm	46.7 μm
-95.1 nm/s	14.5 μm	31.7 μm
Avg of 3 trials:	17.6 μm	



(b)

(c)

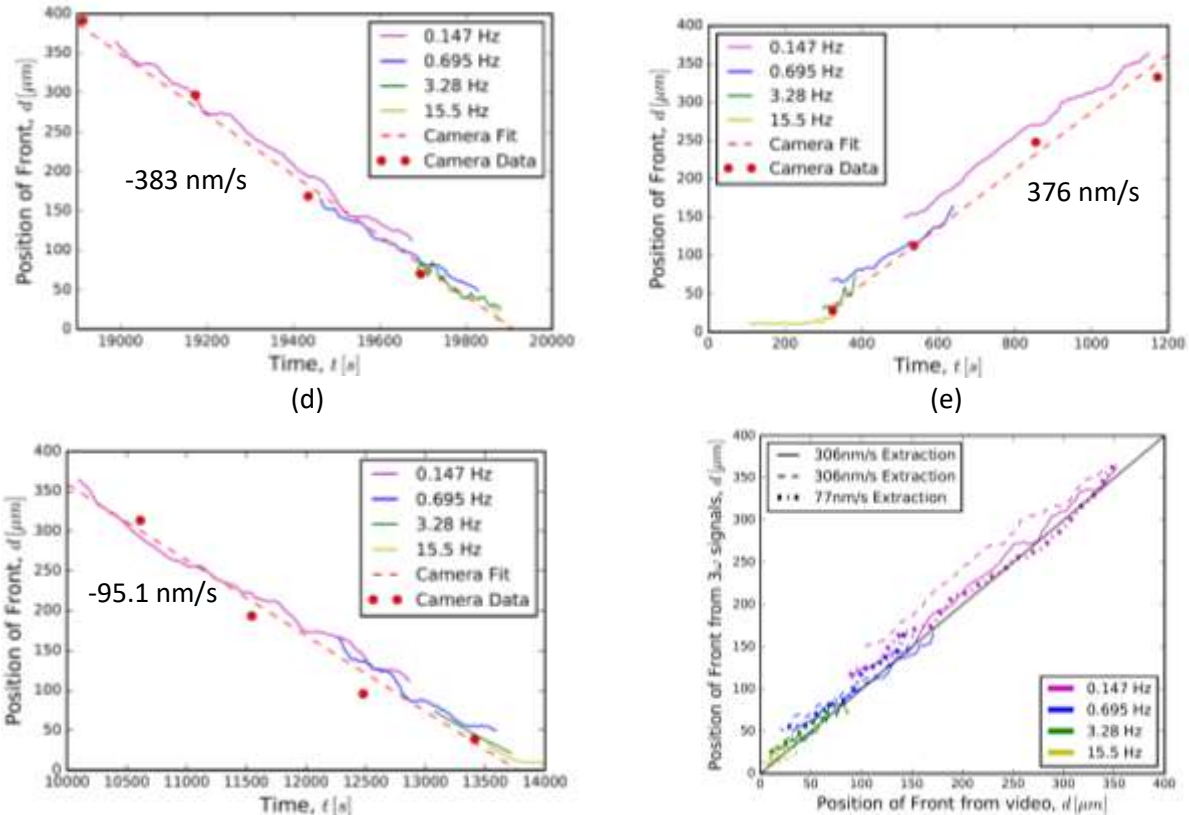


Figure 19: Transient front tracking: determination of front position from out-of-phase 3ω voltage. a) Moving average filtered 0.147 Hz data to be converted into a position measurement; see text). b) Extraction at a rate of 383 nm/s. c) Infusion at a rate of 376 nm/s. d) Extraction at a rate of 95.1 nm/s. e) All 3 trials plotted together, on the axis of position as calculated from 3ω signals versus position as seen by camera. Color corresponds to frequency, as in previous plots, and different trials are plotted with different line styles.

V. Conclusions and outlook

This thesis has demonstrated the ability of the 3ω technique to measure a moving interface between 2 objects of differing thermal conductivity in real time using multiple excitation frequencies. Chapter II showed the ability of the technique to dynamically sense step changes in thermal properties, whether occurring at the heater line or at a distant location. Chapter III demonstrated analytical understanding of interference effects that can occur when exciting a 3ω sensor at multiple frequencies, supported by experimental results. Chapter IV detailed experiments verifying the ability of the technique to measure the location of a moving interface in time, tracking an interface over $350\mu\text{m}$ of motion with RMS error of less than $20\mu\text{m}$, across 3 trials. These results show conceptually the capability of the technique, but do not demonstrate them in a practical system. In order to utilize this technique in the original intended application of cryosurgery, there would be several practical challenges in implementing such a measurement.

The first challenge is alluded to in this thesis: measurement time. Electrical time constant settings on the lock-in amplifier currently limit how quickly a depth measurement can be obtained. Though thermal diffusion times would ultimately limit the speed of measurements, electrical time constants are the dominant limitation on measurement speed. In this thesis, the calculation of position was done after data collection was completed. A moving average was added in post-processing to smooth the data, and a linearly (or otherwise) weighted moving average could be implemented in the hypothetical surgical system. Both of these can decrease the time that is taken to obtain a depth measurement. The lock-in amplifier could even be discarded entirely in favor of customizable signal processing that could occur as the surgery was happening. The processing of the real-time signal is not investigated here, and could be further optimized, utilizing the understanding of frequency interference from Chapter II of this thesis.

The real system of cryosurgery presents other challenges as idealizations are removed from the experiment performed in Chapter IV. In the sensors on balloons used by Natesan et al [25], the geometry is not consistent with the idealization of a sensor that is long compared to thermal penetration depth, and the measurement occurs on a curved substrate. Additionally the cooled nitrogen flowing through the balloon will introduce an additional heat flux into the problem. This is to say these aspects of the real system represent deviations from previously studied geometries, and present enough analytical complexity that numerical modeling is the most obvious path to get information needed to convert real-time voltages to a spatial measurement of depth. Obviously, extensive testing would also be needed before in-situ measurements could be performed practically during a surgery. All of the work here considers a single heater line, and in Chapter IV cumulates with tracking of an interface moving in 1 dimension. With more heater lines, more information can be gained in multiple dimensions. Conceptually similar to Mishra, et al [24], multiple heater lines could be used to probe multiple dimensions of a sample, and determine generate more information about the thermal conductivity in specified regions. Significant computational effort would be needed to convert 3ω data into useful information, but similar ideas have already been used for defect testing in materials [7]. Finally, the enthalpy of phase change that was encountered in Chapter III would be of crucial importance in the cryosurgical application. A better understanding of how this affects the temperature rise at the heater line (and therefore the third harmonic voltage) would be needed before this technique could be implemented in a surgical application.

Broadly speaking, the 3ω technique shows potential for a technique that can measure more than a steady state thermal conductivity of a material. This thesis demonstrated proof of concept of several of these measurement capabilities. With additional work targeted towards optimization for applications, this technique could be used to make in-situ measurements that would otherwise not be possible.

References

- [1] S. Gustafsson, "Transient plane source techniques for thermal conductivity and thermal diffusivity measurements of solid materials," *Review of Scientific Instruments*, vol. 62, no. 3, pp. 797-804, 1991.
- [2] C. Paddock and G. Eesley, "Transient thermoreflectance from thin metal films," *Journal of Applied Physics*, vol. 60, no. 1, pp. 285-290, 1986.
- [3] A. Schmidt, R. Cheaito and M. Chiesa, "A frequency-domain thermoreflectance method for the characterization of thermal properties," *Review of Scientific Instruments*, vol. 80, no. 9, 2009.
- [4] D. Cahill, "Thermal conductivity measurement from 30 to 750 K: the 3 omega method," *Review of Scientific Instruments*, vol. 61, p. 802, 1989.
- [5] M. Ozisik and H. Orlande, *Inverse Heat Transfer*, Boca Raton: Taylor and Francis Group, LLC, 2000.
- [6] T. Nguyen, D. Hao, P. Lopez, F. Cremer and H. Sahli, "Thermal infrared identification of buried landmines," *SPIE*, vol. 5794, no. 1, 2005.
- [7] D. Wu and G. Busse, "Lock-in thermometry for nondestructive evaluation of materials," *Rev. Gen. Therm.*, pp. 693-703, 1998.
- [8] W. Liao and Y. Li, "An automated radiographic NDT system for weld inspection: part II - flaw detection," *NDT&E International*, vol. 31, no. 3, pp. 183-192, 1998.
- [9] P. Zhao and J. Heinrich, "Front-tracking finite element method for dendritic solidification," *Journal of computational Physics*, vol. 173, no. 1, pp. 765-796, 2001.
- [10] H. Natesan, W. Hodges, J. Choi, S. Lubner, C. Dames and J. Bischof, "A Micro-Thermal Sensor for Focal Therapy Applications," *Scientific Reports*, vol. 6, p. 21395, 2016.
- [11] K. Kuck and A. Furnkrantz, "Cryoballoon Ablation of Atrial Fibrillation," *Journal of Cardiovascular Electrophysiology*, vol. 21, pp. 1427-1431, 2010.
- [12] H. Natesan, L. Tian, J. Rodgers and J. Nischof, "A Micro-Thermal Sensor for Cryoablation Balloons," *[In Preparation]*.
- [13] C. Dames, "Resistance temperature detectors," in *Encyclopedia of Micro- and Nano-fluidics*, Berlin, Springer-Verlag, 2008, pp. 1782-1790.
- [14] N. Birge and S. Nagel, "Wide-frequency specific heat spectrometer," *Review of Scientific Instruments*, vol. 58, no. 8, pp. 1464-1470, 1987.

- [15] A. M. J. Schiffres, "Improved measurement of thermal conductivity in liquid, gasses, and powders using a metal-coated optical fiber," *Review of Scientific Instruments*, vol. 82, p. 064903, 2011.
- [16] A. Borca-Tasciuc, A. R. Kumar and G. Chen, "Data reduction in the 3 omega method for thin-film thermal conductivity determination," *Review of Scientific Instruments*, no. 72, p. 2139, 2001.
- [17] A. Jacquot, B. Lenoir, M. Stolzer and J. Meusel, "Numerical simulation of the 3 omega method for measuring the thermal conductivity," *Journal of Applied Physics*, vol. 91, p. 4733, 2002.
- [18] Stanford Research Sytems, *Model SR830 Lock-In Amplifier*, Sunnyvale: Stanford Reserach Systems, 2011.
- [19] Z. I. AG, *HF2 User Manual*, 2012.
- [20] C. Dames and G. Chen, "1, 2, and 3 omega methods for measurements of thermal properties," *Review of Scientific Instruments*, vol. 76, p. 124902, 2005.
- [21] C. Dames, "Chapter 2: Measuring the Thermal Conductivity of Thin Films: 3 Omega and Related Electrothermal Techniques," in *Annual Review of Heat Transfer*, Begell House, 2013.
- [22] K. Moon, Y. Jeong and S. Kwun, "The 3 omega technique for measuring dynamic specific heat and thermal conductivity of a liquid of solid," *Revie of Scientific Instruments*, vol. 67, no. 29, pp. 29-35, 1996.
- [23] F. Chen, J. Shulman, C. Chu and G. Nolas, "Thermal conductivity under hydrostatic pressure using the 3 omega method," *Review of Scientific Instruments*, vol. 75, no. 11, p. 4578, 2004.
- [24] D. Oh, A. Jain, J. Eaton, K. Goodson and J. Lee, "Thermal conductivity measurement and sedimentation detectionof aluminum oxide nanofluids using the 3 omega method," *International Journal of Heat and Fluid Flow*, vol. 28, pp. 1456-1461, 2008.
- [25] B. Park, N. Yi, J. Park, Y. Kim and D. Kim, "Development of a thermal sensor to probe cell viability and concentration in cell suspensions," *AIP Advances*, vol. 4, p. 047120, 2014.
- [26] S. Lubner, J. Choi, G. Wehmeyer, B. Waag, V. Mishra, H. Natesan, J. Bischof and C. Dames, "Reusable bi-directional 3 omega sensor to measure thermal conductivity of 100-um thick biological tissues," *Review of Scientific Instruments*, no. 86, p. 014905, 2015.
- [27] D. Cahill, "Cahill Research Group - Software and Data," [Online]. Available: <http://cahill.matse.illinois.edu/software-and-data/>. [Accessed 10 December 2018].
- [28] D. Lide, *CRC Handbook of Chemistry and Physics*, 90th Edition, CRC Press, 2009.

- [29] M. Zhang, Z. Che, J. Chen, H. Zhao, Y. L. Yang, Z. Zhong and J. Lu, "Experimental Determination of Thermal Conductivity of Water-Agar Gel at Different Concentrations and Temperatures," *Journal of Chemical and Engineering Data*, no. 56, pp. 859-864, 2010.
- [30] CINDAS LLC, "Thermophysical Properties Database," [Online]. Available: <https://cindasdata.com/>. [Accessed 5 February 2018].
- [31] T. Bergman, A. Lavine, F. Incropera and D. Dewitt, *Fundamentals of Heat and Mass Transfer*, Jefferson City: John Wiley and Sons, Inc., 2011.
- [32] V. Mishra, C. Hardin, H. Garay and C. Dames, "a 3 omega method to measure an arbitrary anisotropic thermal conductivity tensor," *Review of Scientific Instruments*, vol. 86, no. 054902, 2015.
- [33] S. R. Choi, J. Hong and D. Kim, "A micromachined AS thermal sensor for monitoring the liquid-gas interface in a microchannel," *Sensors and Actuators A: Physical*, vol. 150, p. 40, 2009.
- [34] N. Birge, "Specific-heat spectroscopy of glycerol and propylene glycol near the glass transition," *Physical Review B*, vol. 34, no. 3, pp. 1631-1642, 1986.